Materials Today Bio 35 (2025) 102477

Contents lists available at ScienceDirect

Materials Today Bio

journal homepage: www.journals.elsevier.com/materials-today-bio

Cu-doped dendritic biodegradable nanoplatforms for augmenting cuproptosis and tumor-starvation therapy through mitochondrial metabolic cascade modulation

Han Shi [a,b,1], Zhiqiang Xie [b,c,1], Junrong Zhang [b,d,1], Fengchun Lu [a], Haoteng Luo [e], Pengfei Guo [f], Meichen Jiang [g], Zongqi Weng [d], Xin Luo [a], Bing Chen [b,2,*], Heguang Huang [a,b,2,**], Tianhong Teng [a,b,***,2]

[a] Department of General Surgery, Fujian Medical University Union Hospital, Fuzhou, 350001, China
[b] Key Laboratory of Nanomedical Technology (Education Department of Fujian Province), Department of Pharmaceutical Analysis, School of Pharmacy, Fujian Medical University, Fuzhou, 350122, China
[c] Department of Clinical Laboratory, Fujian Medical University Union Hospital, Fuzhou, 350001, China
[d] Department of Emergency Surgery, Fujian Medical University Union Hospital, Fuzhou, 350001, China
[e] Department of Critical Care Medicine, Fujian Medical University Union Hospital, Fuzhou, 350001, China
[f] Department of Electronic Science, Fujian Provincial Key Laboratory of Plasma and Magnetic Resonance, Xiamen University, Xiamen, 361005, China
[g] Department of Pathology, Fujian Medical University Union Hospital, Fuzhou, 350001, China

ARTICLE INFO

Keywords:
Functional materials
Bioinspired
Metabolism reprogramming
Branched-chain amino acid
Cuproptosis

ABSTRACT

Reprogramming of branched-chain amino acid (BCAA) metabolism is a key mechanism promoting pancreatic cancer progression. While gabapentin (Gp) can inhibit BCAA catabolism by targeting branched-chain amino acid aminotransferase 1 (BCAT1), its efficacy is limited by inefficient delivery and compensatory mitochondrial metabolism. To address this, we developed a novel copper ionophore-functionalized mesoporous silica nanoplatform (XQ/Gp@CMSNs) for synergistic cuproptosis and tumor-starvation therapy. The designed nanoparticles exhibit excellent pancreatic cancer-targeting capability via XQ-2d aptamer modification and acid-responsive drug release within the tumor microenvironment. Upon internalization, XQ/Gp@CMSNs simultaneously induce mitochondrial copper overload and disrupt BCAA metabolism, leading to dihydrolipoamide S-acetyltransferase (DLAT) oligomerization, ferredoxin 1 (FDX1) downregulation, and tricarboxylic acid (TCA) cycle suppression. Both *in vitro* and *in vivo* studies demonstrated potent antitumor efficacy with minimal systemic toxicity. Metabolomic analyses further confirmed synergistic BCAA metabolic inhibition and copper-induced mitochondrial dysfunction. This work presents a promising metabolic intervention strategy for pancreatic cancer through targeted nanomedicine.

1. Introduction

Pancreatic ductal adenocarcinoma (PDAC) is one of the most aggressive and deadly cancers with a dismally low five-year survival rate of only 13 % [1,2]. It often results in a unique metabolic profile that supports rapid tumor growth, evasion of apoptosis, and invasion of surrounding tissues. Branched-chain amino acids (BCAAs), including leucine, isoleucine, and valine, critical for protein synthesis, energy

* Corresponding author. School of Pharmacy, Fujian Medical University, China.
** Corresponding author. Fujian Medical University Union Hospital, China.
*** Corresponding author. Fujian Medical University Union Hospital, China.
E-mail addresses: shi.fjmu@outlook.com (H. Shi), xiezhiqiang@fjmu.edu.cn (Z. Xie), junrongzhang@fjmu.edu.cn (J. Zhang), fengchun160@163.com (F. Lu), luohaoteng@fjmu.edu.cn (H. Luo), pengfeiguo_xmu@163.com (P. Guo), jiangmeichen@126.com (M. Jiang), 13860655699@163.com (Z. Weng), luoxin980225@163.com (X. Luo), BingChen_001@126.com, BingChen_001@fjmu.edu.cn (B. Chen), heguanghuang25@126.com (H. Huang), tianhongteng24@fjmu.edu.cn (T. Teng).
[1] Han Shi, Zhiqiang Xie and Junrong Zhang have contributed equally to this work.
[2] Tianhong Teng, Heguang Huang and Bing Chen are co-corresponding authors.

https://doi.org/10.1016/j.mtbio.2025.102477
Received 10 August 2025; Received in revised form 15 October 2025; Accepted 27 October 2025
Available online 28 October 2025

metabolism, and physiological regulation. They are converted into branched-chain keto acids (BCKAs) by BCAT and then decarboxylated by the branched-chain α-keto acid dehydrogenase complex (BCKDHC) to produce acetyl-CoA and succinyl-CoA, which are essential for the TCA cycle [3,4]. The metabolism reprogramming of BCAAs helps cancer cells thrive in nutrient-poor microenvironments and influences the surrounding cells and stromal components, further supporting tumor growth [5]. Targeting the BCAAs metabolism pathway may disrupt the metabolic support that pancreatic tumors rely on, inhibit proliferation and metastasis, making it a promising therapeutic strategy in tumor starvation therapy [6].

Chemotherapy, which serves as the primary adjuvant treatment for PDAC, has proven effective in delaying tumor recurrence and improving survival rates [7]. However, the monolithic pharmacological mechanism and significant systemic toxicity often become a pivotal factor in tumor recurrence and treatment failure [8,9]. Therefore, there is a pressing need for the development of innovative high-targeting drugs that harness diverse antitumor mechanisms, aiming to mitigate systemic toxicity while providing multiple anticancer options, ultimately overcoming the current therapeutic challenges in pancreatic cancer [10] [68].

Gabapentin is a common inhibitor of BCAT1, which can effectively inhibit the transamination metabolism of BCAAs [11,12]. Studies have shown that the upregulation of BCAT1 promotes cancer cell proliferation, differentiation, and metastasis [13,14], whereas the inhibition of BCAT1 not only suppresses BCAAs catabolism but also enhances reactive oxygen species (ROS) production through sphingolipid metabolism, thereby inducing cell apoptosis and ultimately inhibiting tumor growth [15–17]. Mitochondria provide ATP and precursors to facilitate the oxidation of BCAAs and other metabolic pathways, which play vital roles in BCAAs metabolism [18,19]. Targeting inhibition of BCAT1 can exploit the dependence of cancer cells on metabolic reprogramming, leading to selective toxicity and a reduction in energy supply and growth support for tumors [20,21]. This presents unique opportunities for targeted cancer therapies.

The dysregulation of copper homeostasis can compromise the metabolic integrity of cancer cells, leading to oxidative stress through the production of ROS, ultimately triggering apoptotic, necrotic, or cuproptotic cell death pathways [22,23]. Furthermore, as the primary organelles where cuproptosis occurs, excessive Cu^{2+} in mitochondria disrupts the mitochondrial TCA cycle by promoting abnormal oligomerization of dihydrolipoamide acetyltransferase (DLAT), triggering mitochondrial proteotoxic stress and ultimately leading to the occurrence of cuproptosis [24–26]. Intriguingly, as the TCA cycle serves as a downstream pathway of BCAAs metabolism, cuproptosis synergizes with gabapentin to block BCAAs metabolic reprogramming in pancreatic cancer cells. Therefore, targeted enrichment of copper-containing drugs within tumor tissues and the avoidance of drug enrichment in normal cells could effectively induce cuproptosis in pancreatic cancer cells and synergistically inhibit BCAAs metabolism, thereby achieving the dual effects of "enhanced efficacy and reduced toxicity" [27].

Transferrin receptor 1 (TFRC1, CD71) is a type II transmembrane glycoprotein that plays a crucial role in the metabolism of iron, copper, and other metal ions [28]. Additionally, TfR1 is often overexpressed in many types of cancer cells because of their heightened metal ion demands for rapid growth and proliferation, making TfR1 a promising target for tumor-targeted therapies [29,30]. Aptamers can selectively bind to specific target molecules and can be conjugated to drug delivery systems to enhance the targeting of therapeutic agents [31–33]. XQ-2d is an adapter with high affinity for CD71, selected through Systematic evolution of ligands by exponential enrichment (SELEX). It exhibits relative stability and low immunogenicity [34]. Our previous research revealed that the conjugation of XQ-2d with nanocarriers can significantly enhance the active targeting capability for pancreatic cancer [35, 36].

Recent studies have convincingly demonstrated the therapeutic potential of copper-based nanoplatforms in oncology. For instance, Xu et al. developed copper-based nanoparticles that significantly amplify endoplasmic reticulum stress and oxidative stress, achieving remarkable antitumor efficacy through synergistic multimodal cell death pathways [37,38]. Separately, Zhang et al. engineered a peptide-copper self--assembled nanoparticle that reprograms tumor glycolytic metabolism to enhance cellular susceptibility to copper ions [39]. Distinct from these approaches, this study presents XQ-2d-modified copper-doped mesoporous silica nanoparticles (XQ/Gp@CMSNs) as a targeted delivery vehicle for gabapentin [40,41]. These nanoparticles can actively target pancreatic cancer cells and exhibit acid-responsive release characteristics within the tumor microenvironment (TME). After intravenous administration, these compounds effectively accumulate and are released at the tumor site, facilitating the uptake of Cu^{2+} and gabapentin by pancreatic cancer cells (Scheme 1). With both cellular and animal models, we confirmed metabolic alterations in pancreatic cancer cells and the occurrence of cuproptosis. Additionally, metabonomic analysis was also carried out to study the correlation between BCAAs metabolic alterations and the prognosis of patients with PDAC through the use of clinical samples. Furthermore, a xenograft tumor model was used to elucidate metabolic changes following drug intervention. Overall, our study offers a novel tumor-starvation therapy strategy for pancreatic cancer.

2. Results and discussion

2.1. Hyperactive BCAAs metabolism in PDAC impacts prognosis

To eliminate the influence of individual metabolic differences, LC–MS metabolomics analysis was conducted on paired samples from 24 patients: cancerous tissues (PDAC group) and adjacent noncancerous tissues (control group). As shown in the heatmap in Fig. 1a and S1, significant metabolite changes were detected between PDAC samples and adjacent noncancer samples, confirming that notable metabolic alterations occurred. Specifically, the levels of BCAAs (leucine, isoleucine, and valine) in pancreatic cancer samples were significantly increased (Fig. 1b), indicating that BCAAs metabolic reprogramming had occurred. To investigate whether the abnormal metabolism of BCAAs in PDAC affects prognosis, we collected postoperative tumor samples and follow-up data from 91 pancreatic cancer patients who were treated from May 2017 to August 2019. By conducting metabolomic analysis, we obtained BCAAs expression levels. On the basis of BCAAs levels, 91 PDAC patients were divided into a high BCAAs group (44 patients) and a low BCAAs group (47 patients) via hierarchical clustering (Fig. 1c). Through metabolite screening, 38 differentially abundant metabolites were identified (Fig. 1d), indicating significant metabolic differences in the cancerous tissues between the two groups. Using follow-up data from two groups of patients for KM survival analysis, we further confirmed that patients with higher intracellular BCAAs levels presented a significantly increased risk of postoperative survival, indicating a significant increase in demand for BCAAs to meet proliferation requirements ($p < 0.05$, Fig. 1e). Moreover, no significant differences in patient characteristics were observed between the two groups (Table S1). These observations led us to hypothesize that inhibiting BCAAs metabolism in PDAC may represent a promising therapeutic strategy to improve patient prognosis.

2.2. Gabapentin inhibits BCAT1 expression In vitro

BCAAs can provide abundant substrates for oxidative metabolism under the transamination of BCAT in PDAC. The resulting BCKAs play vital roles in tumor cells, including sustaining protein synthesis, enhancing the metabolite pool of the TCA cycle, and increasing oxidative phosphorylation, which are intricately linked to tumor proliferation, invasion, and metastasis [42]. The use of nanomedicine to precisely deliver gabapentin to interfere with BCAAs metabolism in tumors holds

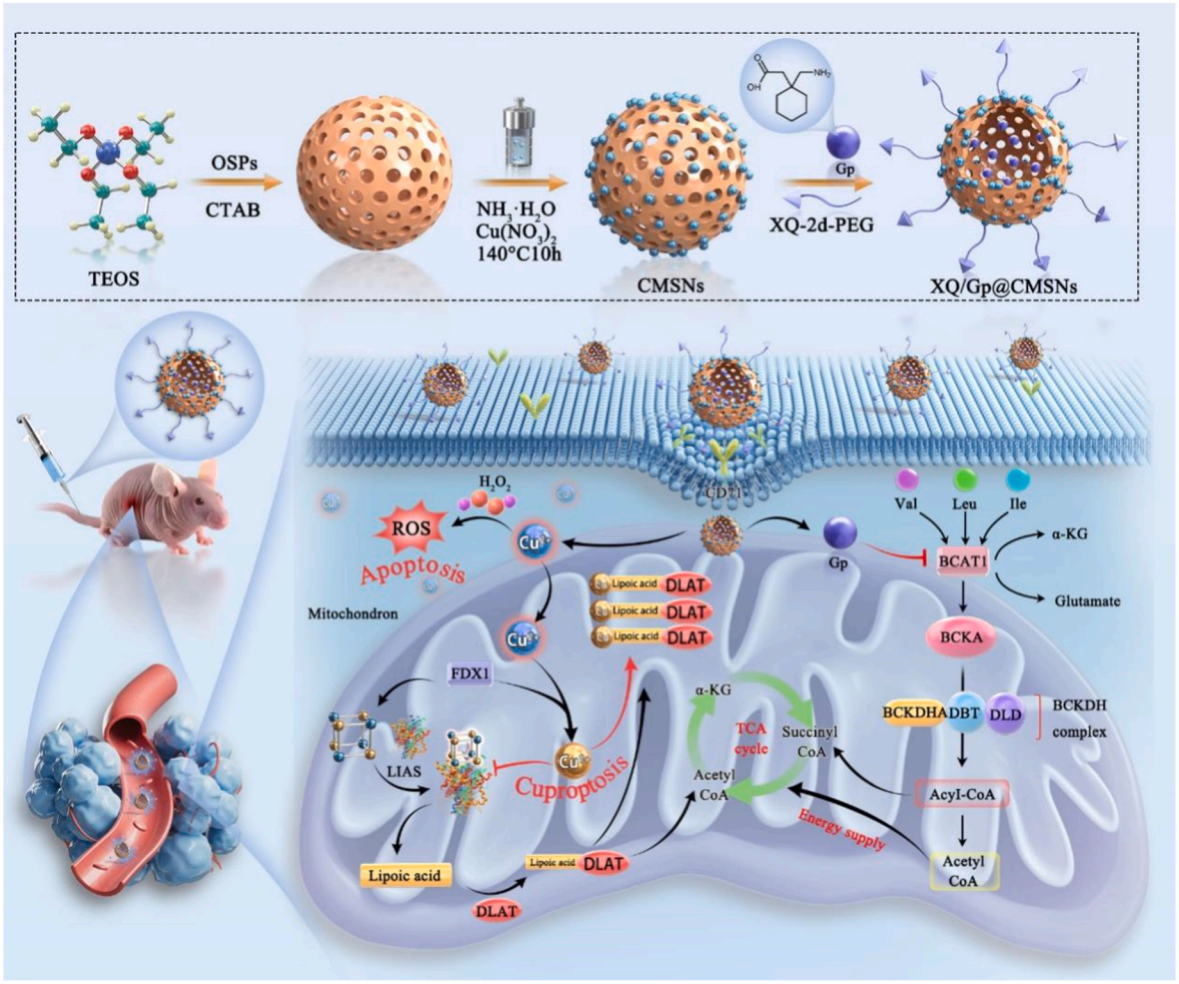

Scheme 1. Synthesis and structural schematic diagram of XQ/Gp@CMSNs. XQ/Gp@CMSNs effectively target and enrich pancreatic cancer tissues, facilitating their internalization into tumor cells and impacting their mitochondria. This results in the induction of cuproptosis and the inhibition of BCAAs metabolism, providing a synergistic treatment strategy for PDAC.

great promise. To assess its influence on BCAT1 expression in PDAC, an *in vitro* experiment in which pancreatic cancer cells were cocultured with gabapentin was conducted. Subsequent Western blot (WB) analysis revealed a notable decrease in BCAT1 expression levels (Fig. S2).

2.3. Construction and characterization of Gp@CMSN nanoparticles

To devise a carrier for precise drug delivery to tumor cells, mesoporous silica nanoparticles (MSNs) were synthesized via the Stöber method (Fig. 2a) [43]. The hydrated particle size was measured to be 128.9 nm. Transmission electron microscopy (TEM) images and dynamic light scattering (DLS) revealed well-dispersed spherical structures with diameters of approximately 100 nm (Fig. 2b–d). Under an alkaline environment, Cu^{2+} can undergo a deprotonation reaction with the Si-OH groups on the surface of MSNs, forming Si-O-Cu covalent coordination bonds. To achieve the co-delivery of copper ions and nanocarriers, Copper-doped mesoporous silica nanoparticles (CMSNs) were subsequently synthesized through a hydrothermal method (Fig. 2a).

TEM combined with Scanning electron microscopy (SEM) revealed a uniform hollow urchin-like structure. Compared with that of MSNs, the particle size increased due to the formation of surface dendrite structures (Fig. 2e–g). Selected area electron diffraction (SAED) indicated a tendency for weaker crystallization in the copper-doped particles than in the MSNs (Fig. 2h–S3). High-angle annular dark-field (HAADF) imaging further demonstrated the uniform distribution of Cu, O, and Si across the particle shell (Fig. 2j). A comparison of the X-ray diffraction (XRD) patterns of the MSNs and CMSNs with those of the standard CuSiO3·xH2O cards confirmed that the product was hydrated copper silicate (Fig. 2i). Inductively coupled plasma–mass spectrometry (ICP–MS) revealed that the mass percentages of Si and Cu in the material were 15.17 % and 31.92 %, respectively. These results suggest that the main component of the material is $CuSiO_3{\cdot}2H_2O$. N_2 adsorption–desorption curves revealed a significant increase in the specific surface area and a slight increase in the mesopore size of the CMSNs compared with those of the MSNs (Fig. 2k and l), which effectively enhanced the drug loading capacity of the material. X-ray photoelectron spectroscopy (XPS) analysis confirmed the elemental composition of the material and revealed the characteristic peaks of Cu^{2+} at 945 and 962.5 eV (Fig. 2m–S4). Owing to its hollow urchin-like structure, gabapentin was effectively loaded through physical adsorption, with a drug loading rate of 31.8 wt %, as determined by high-performance liquid chromatography (HPLC).

2.4. TME-responsive drug liberation of Gp@CMSNs

Given that a mildly acidic environment can induce the cleavage of Cu-O bonds, we hypothesized that CMSNs may exhibit acidity-responsive drug release properties in the TME [44,45]. As illustrated in Fig. 3a, Cu^{2+} catalyzes the decomposition of H_2O_2 to generate ·OH radicals, which in turn oxidize 3,3′,5,5′-tetramethylbiphenyl (TMB) and can be detected with an absorption peak at 650 nm [46,47]. To validate this hypothesis, we observed changes in the number of CMSNs coincubated with H_2O_2 under different pH conditions. No significant ·OH

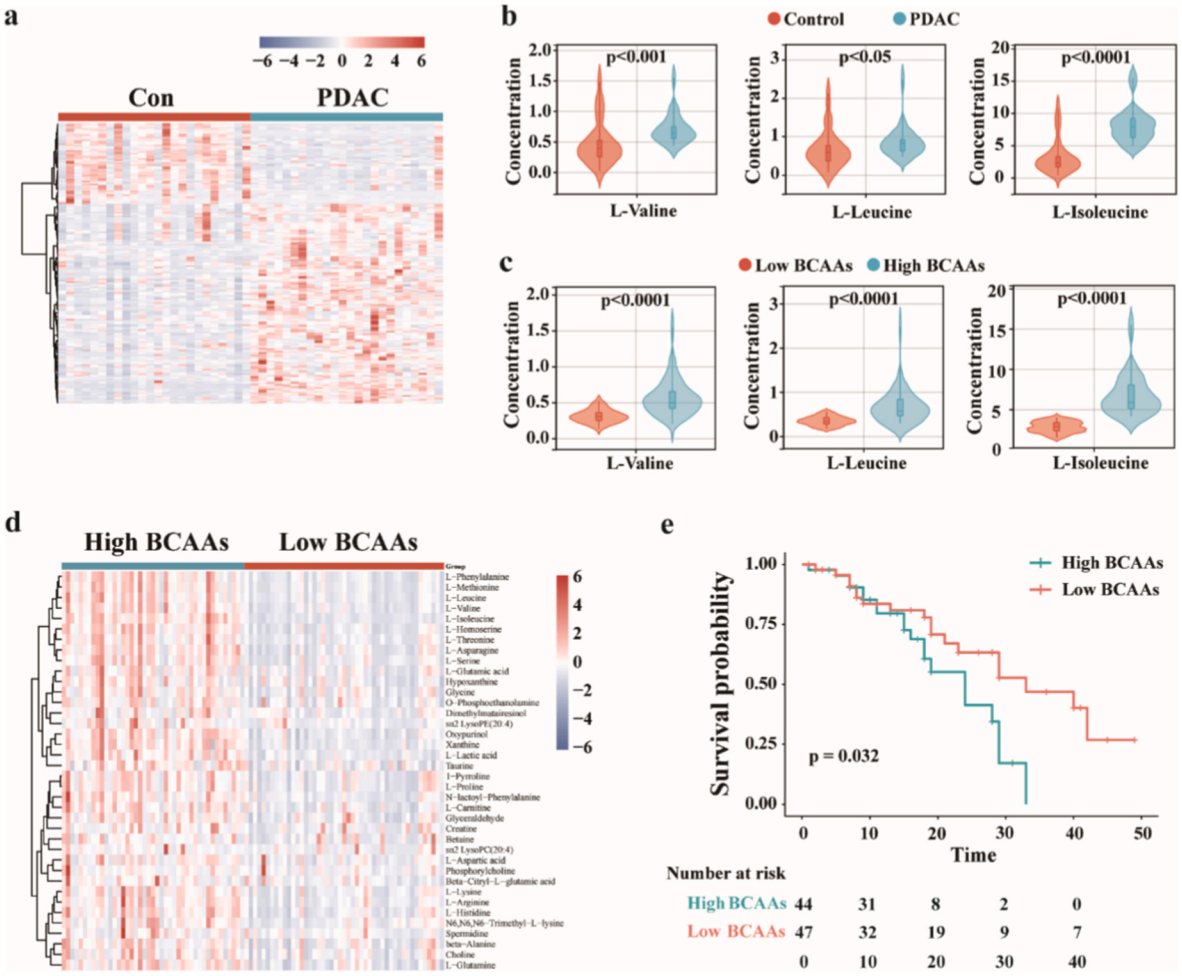

Fig. 1. Patients were divided into high-risk and low-risk groups on the basis of the median expression level of BCAAs. (a) Heatmap displaying the differentially abundant metabolite expression levels between 24 pairs of cancer and adjacent noncancerous tissues, where red indicates high expression and blue indicates low expression. The violin plot shows the relative concentrations of BCAAs in (b) cancerous and adjacent noncancerous tissues, as well as (c) between the high BCAAs and low BCAAs groups. (d) Heatmap illustrating the differentially abundant metabolite expression levels between the high BCAAs and low BCAAs groups. (e) K–M survival curves for the high BCAAs and low BCAAs groups. (For interpretation of the references to color in this figure legend, the reader is referred to the Web version of this article.)

generation was observed at pH 7.4, whereas a prominent color shift was noted at pH 6.5, simulating the TME (Fig. 3b). To further substantiate the capability of CMSNs in generating ·OH, electron spin resonance (ESR) spectroscopy was employed. H_2O_2 (100 μM) was utilized to mimic the TME. Upon the addition of CMSNs to the reaction system, the characteristic ESR signal of ·OH (1:2:2:1) was detected in both pH 7.4 and pH 6.5 media. Notably, the signal intensity was significantly enhanced under acidic conditions (Fig. S5). These results indicate that the CMSNs can effectively release Cu^{2+} in the TME. Measurements of the 24-h cumulative release rates of Cu^{2+} and gabapentin revealed that an acidic environment facilitated the release of both (Fig. 3c and d). To delve deeper into the morphological alterations of Gp@CMSNs under different pH conditions, we incubated the nanoparticles in acidic or neutral PBS for various time intervals and visualized their structure via TEM. After 12 h in an acidic environment, only a few nanospherical structures remained intact, with complete disintegration occurring at 24 h. In contrast, the structural damage to Gp@CMSNs at pH 7.4 was significantly less severe, with a certain degree of particle structure still preserved after 24 h (Fig. 3e). Notably, the extent of nanostructure disruption correlated well with the level of Cu^{2+} release in the PBS. Similarly, the nanoparticles released Cu and Si at a faster rate under mildly acidic conditions than in the neutral SBF, which is attributed to the cleavage of Cu–O bonds upon attack by H^+ (Fig. S6). Collectively, these findings underscore the TME-responsive drug liberation capabilities of Gp@CMSNs. This unique characteristic holds promise for enhancing drug accumulation at tumor sites while mitigating adverse effects in normal tissues [32].

2.5. Synthesis of XQ/Gp@CMSNs

Building upon our previous research, we synthesized XQ/Gp@CMSNs to further augment their biocompatibility and active targeting capabilities. Initially, utilizing the insolubility of gabapentin in ethanol and the covalent binding of Si-O-Si, successful modification of Gp@CMSNs with MaL-PEG-silane was achieved. Through covalent binding between -SH groups and MAL, XQ-2d was subsequently modified on the outermost layer of PEG/Gp@CMSNs to increase its ability to actively target PDAC (Fig. 2a) [36,48,49]. TEM confirmed a slight increase in the particle size of the nanoparticles, and a colloidal structure formed by PEG modification was observed on the surface (Fig. 3f) [50]. The negative zeta potential of the modified nanoparticles increased slightly, which is beneficial for reducing circulatory loss during blood circulation. This is due to the neutralization between negatively charged XQ-2d and positively charged PEG (Fig. 3g). Fourier transform infrared (FTIR) spectroscopy confirmed the PEGylation of the CMSNs and the modification of XQ-2d. The DLS of XQ/Gp@CMSNs is slightly increased

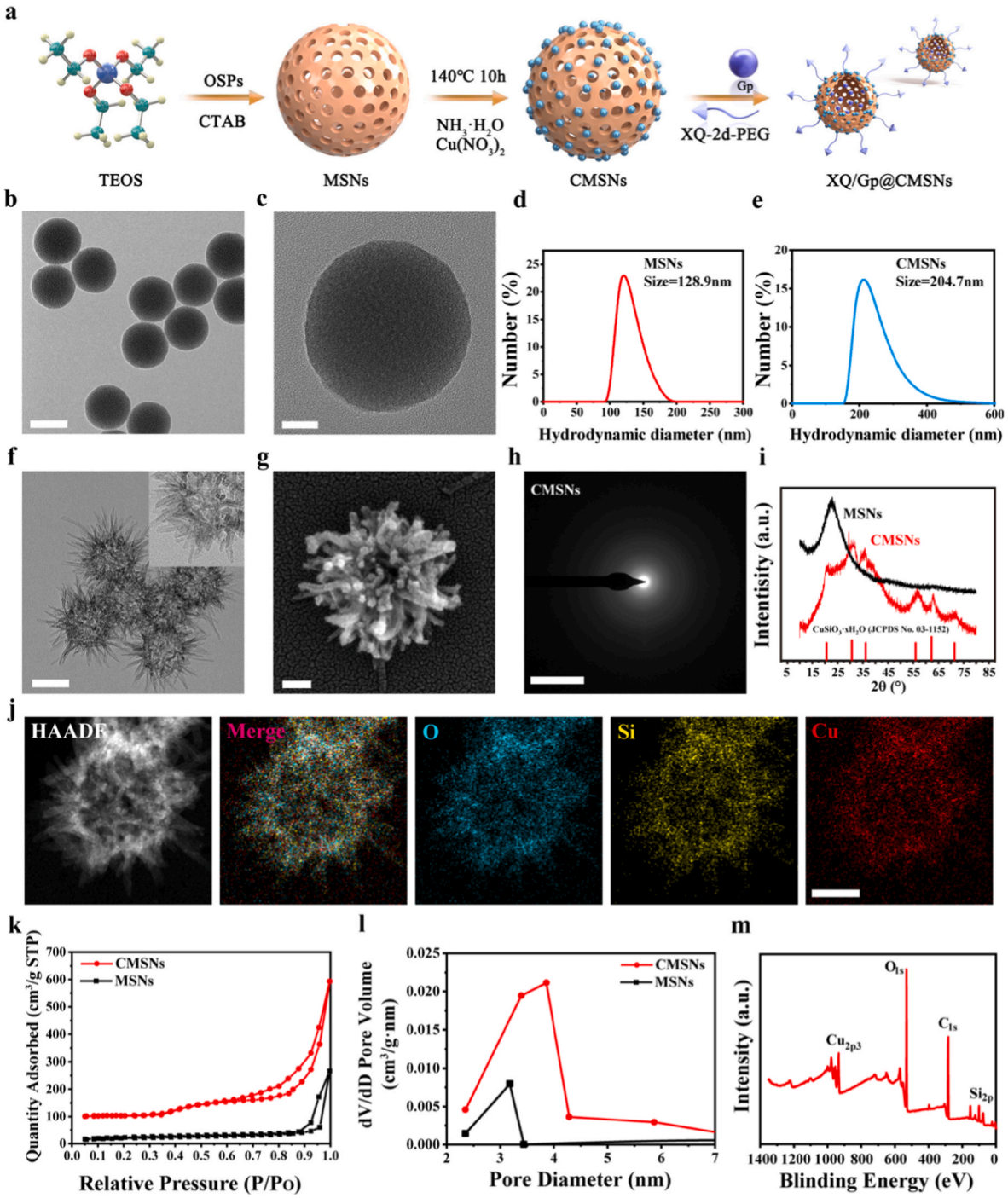

Fig. 2. Structural characterization of the nanoparticles. (a) Synthesis and structural schematic diagram of MSNs, CMSNs, and XQ/Gp@CMSNs. (b, c) TEM image of MSNs; scale bars = 100 nm and 25 nm. The size distributions of the (d) MSNs and (e) CMSNs. (f) TEM and (g) SEM images of CMSNs; scale bars = 100 nm and 50 nm. (h) SAED patterns of CMSNs; scale bars = 10 nm. (i) XRD patterns of MSNs, CMSNs, and $CuSiO_3{\cdot}H_2O$. (j) Dark-field TEM image and corresponding area-elemental mappings of CMSNs; scale bars = 50 nm. (k) N_2 adsorption−desorption isotherms and (l) corresponding pore size distributions of MSNs and CMSNs. (m) XPS spectra of the CMSNs.

compared to CMSNs, which is due to the modification of PEG and XQ-2d (Fig. S7). Compared with CMSNs, PEG/CMSNs presented a vibrational peak at 1680–1620 cm^{-1}, which is the characteristic peak of MAL-PEG-silane (C=C stretching). The characteristic peak of the thioether bond (R-S-R) formed by the covalent binding of -SH with MAL overlaps with the Si-O characteristic peak at 1000–1200 cm^{-1}, manifesting as a deeper peak at 1000–1200 cm^{-1} for XQ/CMSNs than for PEG/CMSNs in the FTIR spectrum (Fig. 3h). The absorbance curves of different particles measured by a UV–Vis spectrophotometer revealed that the characteristic peak of Cy3 at 550 nm for both free ^{Cy3}XQ and ^{Cy3}XQ/CMSNs confirmed the binding of XQ-2d to the CMSNs (Fig. S8). These experiments collectively demonstrate the successful PEGylation of CMSNs and their modification with XQ-2d.

2.6. *In vitro cellular internalization and mitochondrial dysfunction*

Given the specific binding ability of XQ-2d to CD71 on the surface of pancreatic cancer cells, we aimed to determine whether modification

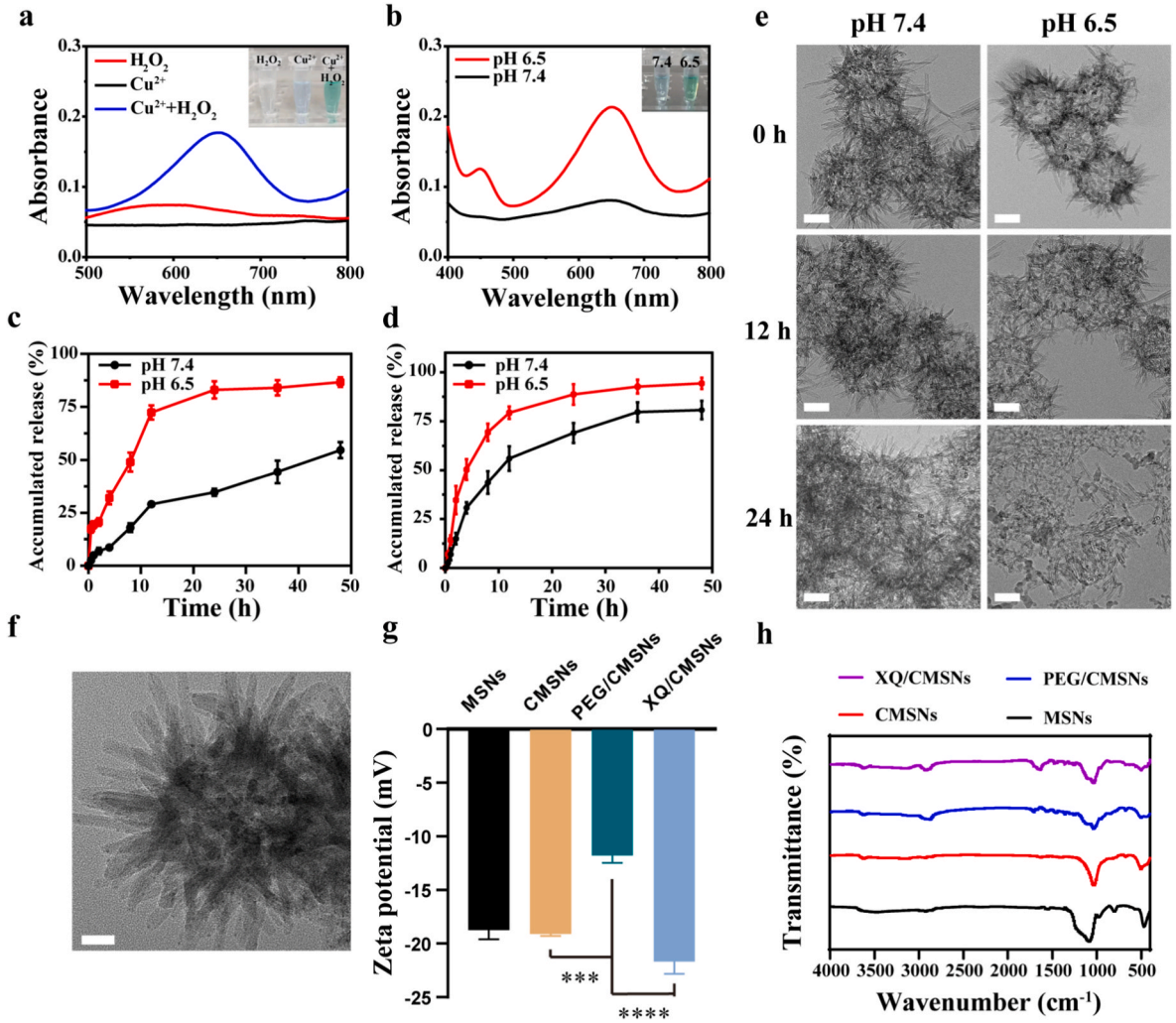

Fig. 3. Acid response characteristics and structural features of the nanoparticles. (a) UV–vis spectra and photographs (inset) of TMB aqueous solutions treated with H_2O_2, Cu^{2+}, or Cu^{2+} plus H_2O_2 for 30 min. (b) Colorimetric detection of •OH generated by CMSNs at different pH values (inset) via the TMB assay. (c) Cumulative Cu and (d) gabapentin release from Gp@CMSNs at different pH values. (e) TEM images of CMSNs after immersion in PBS at various pH values for 0, 12, and 24 h; scale bars = 50 nm. (f) TEM images of XQ/Gp@CMSNs; scale bar = 25 nm. (g) Zeta potential of MSNs, CMSNs, PEG/CMSNs, and XQ/CMSNs. (h) Fourier transform infrared (FTIR) spectra of MSNs, CMSNs, PEG/CMSNs, and XQ/CMSNs. Intergroup comparison was performed using the *t*-test. ***$p < 0.001$, and ****$p < 0.0001$.

with XQ-2d enhances the cellular internalization of nanoparticles. To this end, Cy3-labeled PEG/CMSNs (PEG/$CMSNs^{Cy3}$) and XQ/CMSNs (XQ/$CMSNs^{Cy3}$) were coincubated with pancreatic cancer cells for 3 h and 6 h, respectively, followed by observation via confocal laser-scanning microscopy (CLSM). As shown in Fig. 4a–c, after a 3-h incubation period, no significant red fluorescence was detected in PATU-8988 or BxPC-3 cells treated with PEG/$CMSNs^{Cy3}$. In contrast, notable red fluorescence was observed in the XQ/$CMSNs^{Cy3}$ groups. When the incubation time was extended to 6 h, the cells exposed to PEG/$CMSNs^{Cy3}$ presented only faint fluorescent signals; this strongly contrasted with the prominent signals detected in the cells treated with XQ/$CMSNs^{Cy3}$. These results indicate that pancreatic cancer cells can more efficiently internalize XQ-2d-modified nanoparticles because of the presence of CD71 receptors on their membranes. Furthermore, this internalization capability is time dependent. As mitochondria are the primary site of action for the tumor starvation therapy, confirming the efficient delivery of Cu^{2+} to this organelle is critical. To this end, we quantitatively analyzed the mitochondrial Cu content under different treatment conditions using ICP-MS. As shown in Fig. S9, after incubation for 12 h, the Cu content in the mitochondria treated with XQ/CMSNs was significantly higher than that treated with PEG/CMSNs, in both the PATU-8988 and BxPC-3 cell lines. These findings are of great significance for enhancing drug delivery into tumor cells and mitochondria, thereby improving therapeutic efficacy against malignancies [51].

2.7. *In vitro cytotoxicity experiments*

Given the remarkable cellular internalization capabilities of our nanoparticles, we subsequently assessed the cytotoxic effects of various doses of nanomedicine formulations on pancreatic cancer cells. PATU-8988 and BxPC-3 cells were incubated with different concentrations of nanoparticles or gabapentin for 48 h, and CCK-8 assays were used to evaluate changes in cell viability. Initially, the cells were coincubated with PEG/MSNs across a range of concentration gradients, revealing that even at concentrations as high as 200 μg/mL, the cell viability remained at approximately 80 %. This finding suggests good biocompatibility of the PEG/MSNs (Fig. 4d). Free gabapentin alone exhibited limited cytotoxicity, with significant inhibition of cell viability observed only at 15 mM gabapentin (Fig. 4e). Further investigation into the effects of various copper-doped nanoparticles on cell viability revealed that increasing concentrations led to a reduction in the viability of cells when treated with PEG/CMSNs, PEG/Gp@CMSNs, or their aptamer conjugates. It appears that PEG/Gp@CMSNs displayed stronger cytotoxicity than PEG/CMSNs; this enhanced effect is attributed to the

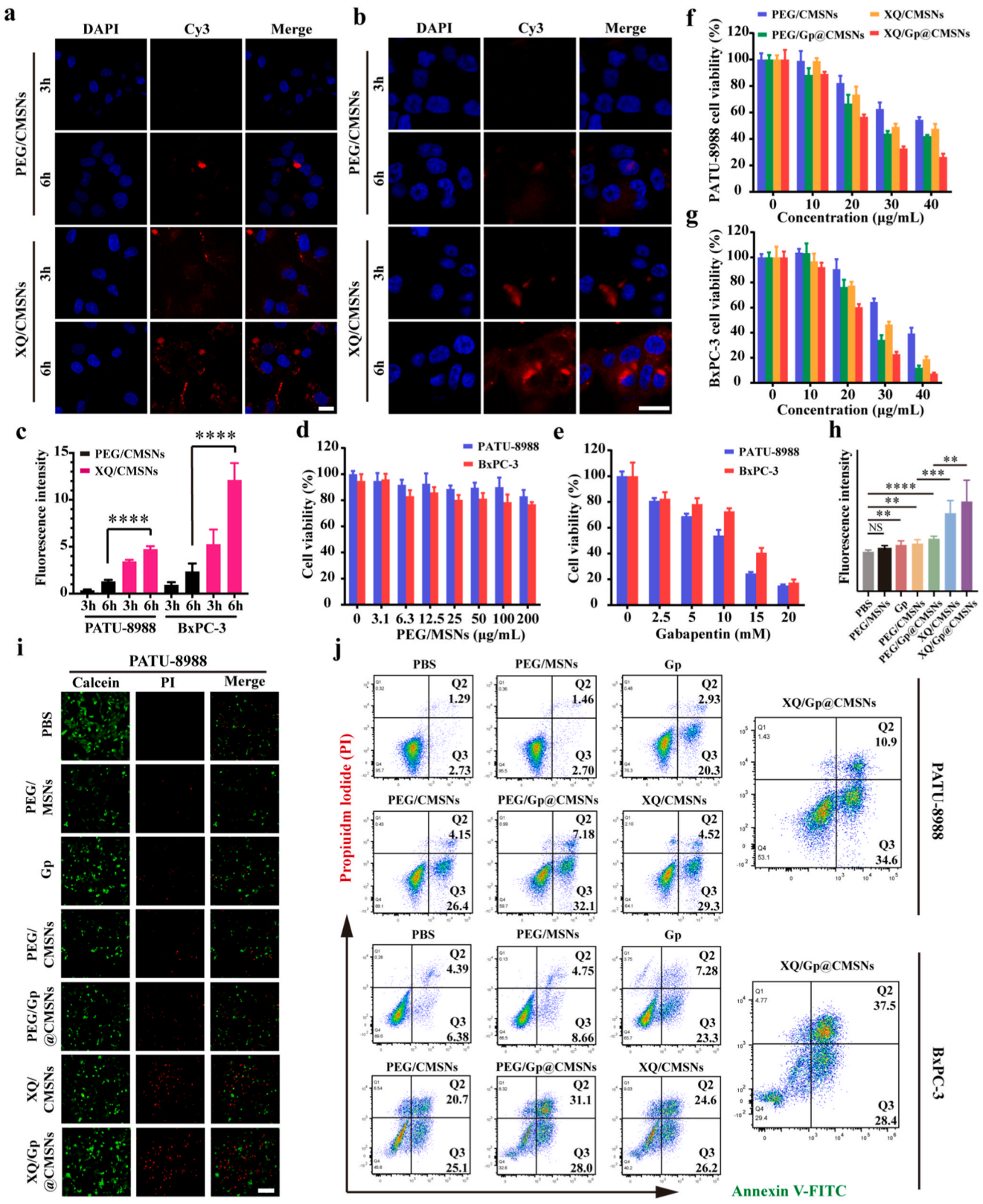

Fig. 4. *In vitro* cellular uptake and cell viability assays. CLSM images of (a) PATU-8988 and (b) BxPC-3 cells incubated with PEG/CMSNs^{Cy3} and XQ/CMSNs^{Cy3} at different time points, with (c) quantification of the corresponding fluorescence intensity (n = 5); scale bar = 20 μm. (d–g) Viability of PATU-8988 and BxPC-3 cells after different treatments under various conditions for 48 h. (i) Fluorescence images of calcein AM (green, live cells) and PI (red, dead cells) contained PATU-8988 cells after incubation with PBS, PEG/MSNs, free gabapentin, PEG/CMSNs, PEG/Gp@CMSNs, XQ/CMSNs, or XQ/Gp@CMSNs for 48 h; scale bars = 100 μm. (h) Fluorescence intensity of PI in PATU-8988 cells after different treatments (n = 5). (j) Flow cytometry analysis of cells subjected to 7 different treatments followed by staining with Annexin−FITC and PI. Intergroup comparison was performed using the *t*-test. ****$p < 0.0001$. (For interpretation of the references to color in this figure legend, the reader is referred to the Web version of this article.)

synergistic toxic impact of gabapentin and Cu^{2+} on the cells. Following modification with XQ-2d, the toxic effects associated with XQ/Gp@CMSNs were further amplified compared with those observed with both PEG/CMSNs and PEG/Gp@CMSNs. At a concentration of 30 μg/mL, these modified nanoparticles inhibited approximately 70 % of PATU-8988 and approximately 80 % of BxPC-3 cell viability, demonstrating their stronger cytotoxic potential (Fig. 4f and g). The mildly alkaline pH value and relatively low levels of H_2O_2 in the normal cellular environment may exert an influence on drug release. The low expression of CD71 on the cell surface may affect the endocytic capacity of nanoparticles. To elucidate the impact of XQ/Gp@CMSNs on the viability of normal cells, XQ/Gp@CMSNs was co - incubated with human cardiomyocytes AC16. The results indicated that, compared with pancreatic cancer cells, the cytotoxicity of XQ/Gp@CMSNs to AC16 cells was markedly lower. At a concentration of 30 μg/mL, AC16 still maintained an average cell viability of 80.7 %, whereas PATU - 8988 and BxPC - 3 exhibited cell viabilities of 32.8 % and 22.8 %, respectively. This further enhances the selective toxicity of XQ/Gp@CMSNs towards cancer cells (Fig. S10). Cell migration experiments demonstrated that, within 24 h, compared with PBS and MSNs, gabapentin mildly inhibited cell migration. Owing to the incorporation of Cu^{2+}, PEG/Gp@CMSNs significantly enhanced the inhibition of cells, and upon modification with XQ-2d, nearly complete inhibition of cell migration was noted (Fig. S11a and S11b). Calcein-AM/PI staining corroborated these findings, with minimal red fluorescence representing dead cells in the PBS groups. Drug groups without aptamer modification showed partial red fluorescence, whereas the XQ/Gp@CMSN groups presented the most pronounced red fluorescence (Fig. 4h, i S12). Flow cytometry analysis of cell apoptosis revealed that, compared with those in the PBS groups, different proportions of apoptotic cells were present in the groups exposed to various drugs. The trends in apoptosis were consistent across different subgroups within both cell lines, with the highest proportions of early and late apoptotic cells observed in the XQ/Gp@CMSN groups (Fig. 4j). PATU-8988 cells predominantly underwent early apoptosis, whereas BxPC-3 cells were mainly in the late apoptotic stage. The potential factors underlying this stage-specific discrepancy may include their differential p53 status, varying expression levels of anti-apoptotic proteins, or differences in drug uptake and metabolism [52,53]. These findings are in line with the CCK-8 and calcein-AM/PI double-staining results. These experimental results demonstrate that gabapentin and CMSNs have synergistic inhibitory effects on the proliferation of PDAC cells and that modification with XQ-2d significantly increases cytotoxicity by increasing the cellular uptake of the nanoparticles.

2.8. Mitochondrial Toxicity and Cuproptosis Induced by Cu^{2+} overload

The increase in Cu^{2+} within cells triggers an increase in ROS via Fenton-like reactions. By employing the DCFH-DA probe to quantify ROS, the XQ/Gp@CMSN group presented the most intense green fluorescence [54]. Conversely, the fluorescence intensity of the PEG/MSN groups was comparable to that of the PBS groups (Fig. 5a–c, S13). Notably, the Gp groups also presented an increase in fluorescence intensity compared with that of the control, which can be attributed to BCAT inhibition stimulating the production of ROS, thereby synergizing with the Fenton-like reaction of Cu^{2+} [15]. This finding elucidates the reason behind the significantly greater cytotoxicity of gabapentin-loaded nanoparticles than of gabapentin alone. Elevated ROS levels lead to increased oxidative stress and mitochondrial dysfunction. Alterations in the mitochondrial membrane potential (MMP) serve as early indicators of mitochondrial damage. JC-1 exists in an aggregated state in normal mitochondria, whereas it shifts to a monomeric form as the MMP decreases [55]. Flow cytometry analysis indicated that PEG/MSNs had negligible effects on the MMP. However, with the incorporation of Cu^{2+}, significant changes in the MMP were evident, as indicated by a notable increase in the proportion of JC-1 monomers. This finding underscores the disruptive impact of Cu^{2+} on mitochondrial function, an effect that was further accentuated by XQ-2d modification (Fig. 5d–f, S14). Interestingly, the use of gabapentin alone also induced mild disruption of the MMP, confirming its role in facilitating ROS production in PDAC. Although PEG/Gp@CMSNs more effectively inhibited cell viability than XQ/CMSNs did in previous experiments, XQ/CMSNs caused more pronounced alterations in the MMP. In addition to generating excessive ROS to impair mitochondria, Cu^{2+} overload also triggers cuproptosis, further exacerbating mitochondrial injury [56]. When Cu^{2+} penetrates mitochondria, it is reduced to Cu^{+} by FDX1. Under the guidance of FDX1, Cu^{+} subsequently binds to DLAT, causing DLAT to oligomerize abnormally. This abnormal oligomerization initiates a cascade of mitochondrial protein toxicity stress, ultimately leading to cell death [25,57]. This mechanism offers a persuasive rationale for the significant increase in JC-1 positivity observed in CMSN-treated cells. To further validate the occurrence of cuproptosis in cells, the expression of cuproptosis-related proteins was examined [58]. Western blotting revealed decreased levels of FDX1 and DLAT in both the PEG/Gp@CMSN and XQ/Gp@CMSN groups compared with those in the PBS and free gabapentin groups (Fig. 5g, h, S15). Considering that FDX1 plays a crucial role in the lipoylation of various mitochondrial proteins, its downregulation and DLAT oligomerization further inhibit downstream pathways of BCAAs catabolism through the TCA cycle [59].

2.9. Active tumor-targeting of XQ/CMSNs In vivo

We confirmed the enhanced uptake of XQ/Gp@CMSNs by tumor cells *in vitro*. To evaluate their efficacy in actively targeting tumors *in vivo*, PEG/CMSNs and XQ/CMSNs were labeled with Cy5.5 and subjected to *in vivo* imaging at various time points to observe the tissue distribution of the nanoparticles. As shown in Fig. 6b, the fluorescence intensity at the tumor site peaked at 24 h postinjection. A comparative analysis between the two groups revealed that XQ/CMSNs presented increased fluorescence intensity at the tumor site across all time points after administration. Notably, 36 h postinjection, the residual fluorescence signal within the tumor of the PEG/CMSN group was markedly weak; conversely, substantial fluorescence accumulation remained evident in the XQ/CMSN group. These findings indicate that XQ-2d modification enhances both the uptake of CMSNs by tumors and prolongs the intratumoral retention time. Tumors and major organs were harvested for *ex vivo* fluorescence imaging analysis 36 h after injection. The results corroborated those observed *in vivo*. Specifically, mouse tumor tissues from the XQ/CMSN group retained a significantly stronger fluorescence signal than those from the CMSN group. Among the major organs examined, fluorescence was noted in the liver, indicating that these nanoparticles are metabolized primarily through the liver (Fig. 6b and c).

2.10. In vivo targeted anti-tumor therapy

Given the excellent cytotoxic effect of XQ/Gp@CMSNs on pancreatic cancer cells *in vitro*, we further investigated the synergistic effects of cuproptosis and the inhibition of BCAAs metabolism *in vivo*. BALB/c nude mice were randomly divided into six groups: the PBS group (group I), the gabapentin group (group II), the PEG/CMSNs group (group III), the PEG/Gp@CMSNs group (group IV), the XQ/CMSNs group (group V), and the XQ/Gp@CMSNs group (group VI). The corresponding formulations were subsequently intravenously injected every two days, and the changes in weight and tumor size were recorded (Fig. 6a). The changes in tumor volume revealed that the inhibitory effect of gabapentin injection (group II) on tumor growth was limited, with no significant reduction compared with that of group I. Tumor growth in groups III and IV was inhibited to some extent. However, after modification with XQ-2d, the antitumor effect *in vivo* was significantly enhanced. In group VI, owing to the targeting ability and combined effect of gabapentin and Cu^{2+}, tumor growth was completely inhibited throughout the entire treatment course (Fig. 6d and e). After 14 days of

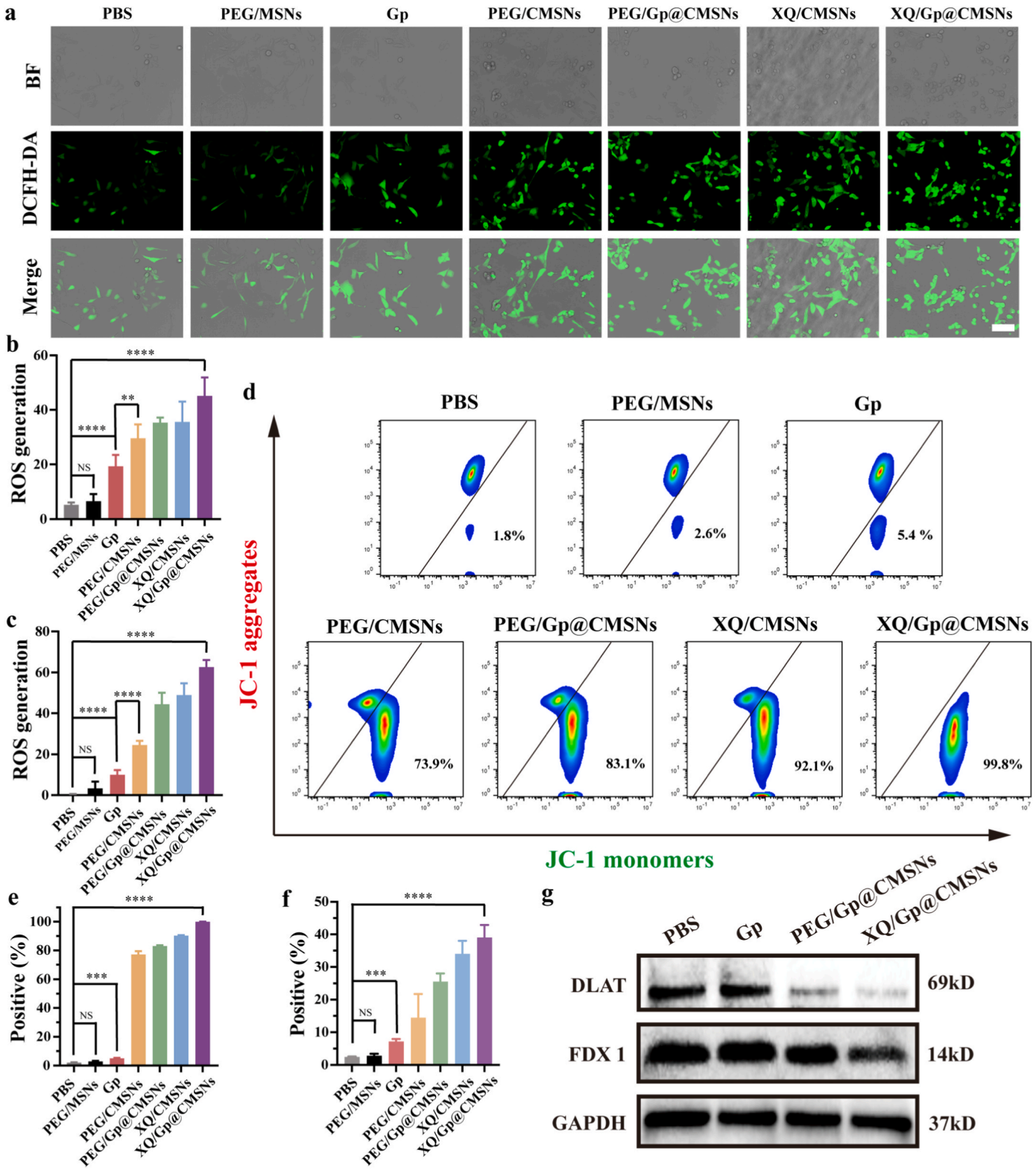

Fig. 5. Toxicity and Cuproptosis Induced by Cu^{2+} *in vitro*. (a, b) CLSM images and corresponding intensity (n = 5) of ROS generation in PATU-8988 cells by staining with DCFH-DA after various treatments; scale bars = 100 μm. (c) Fluorescence intensity of ROS generation in BxPC-3 cells by staining with DCFH-DA after various treatments (n = 5). (d, e) Flow cytometry analysis and corresponding intensities (n = 3) of PATU-8988 cells subjected to 7 different treatments followed by JC-1 staining. (f) Fluorescence intensity of BxPC-3 cells subjected to various treatments followed by JC-1 staining (n = 3). (g) Western blot analyses of cuproptosis-related proteins in PATU-8988 cells subjected to various treatments for 48 h. Intergroup comparison was performed using the *t*-test. NS, not significant, $^{**}p < 0.01$, $^{***}p < 0.001$, and $^{****}p < 0.0001$.

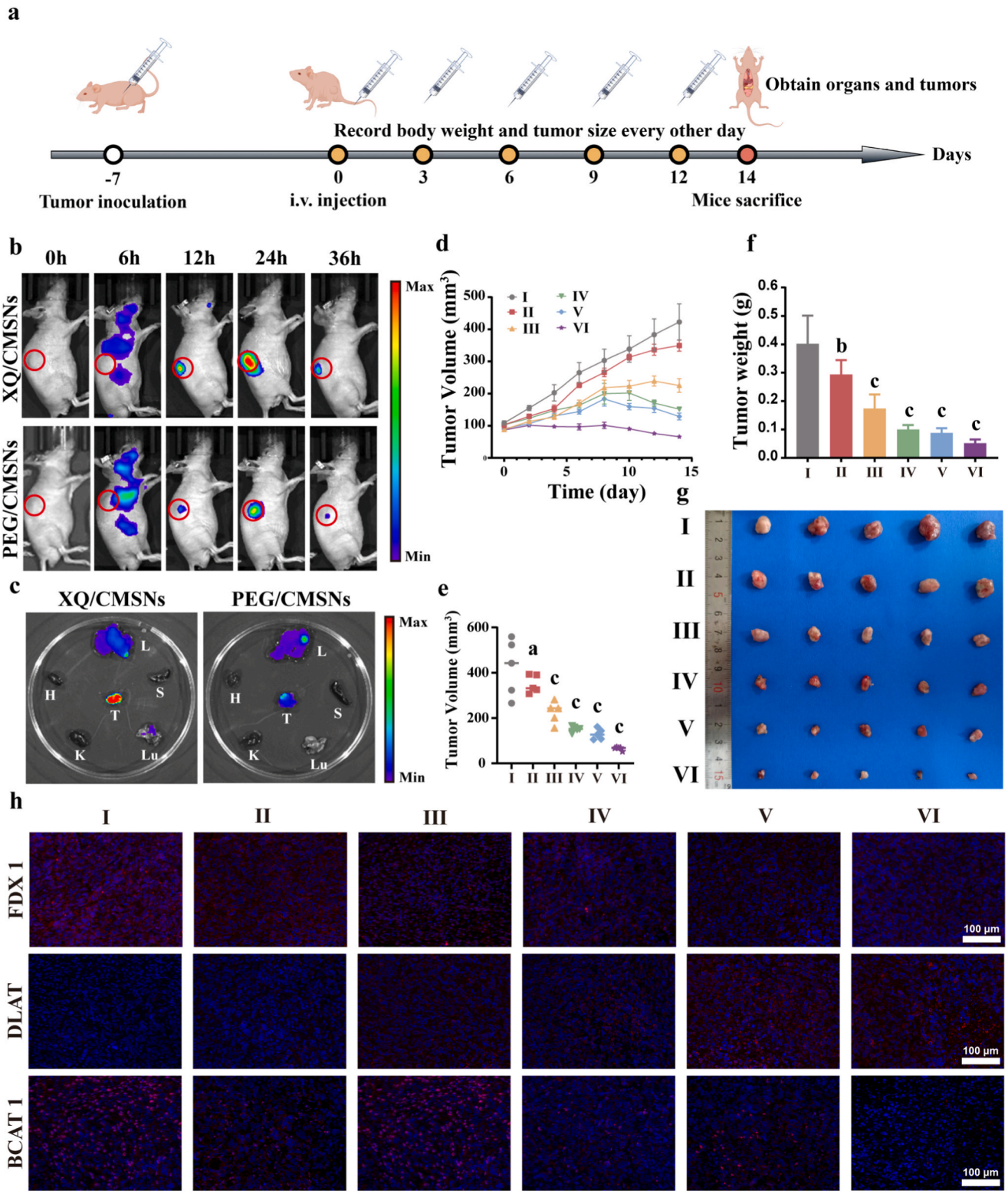

Fig. 6. *In vivo* antitumor effects of XQ/Gp@CMSNs (I: PBS, II: Gp, III: PEG/CMSNs, IV: PEG/Gp@CMSNs, V: XQ/CMSNs, VI: XQ/Gp@CMSNs). (a) Schematic illustration of PATU-8988 tumor xenograft establishment and treatment. (b) *In vivo* fluorescence imaging of PATU-8988 tumor-bearing mice after intravenous injection of Cy5.5-loaded PEG/CMSNs and XQ/CMSNs. The red circles indicate the tumor sites. (c) *Ex vivo* fluorescence images of tumor tissues and major organs collected from mice at 36 h postinjection of Cy5.5-loaded PEG/CMSN and XQ/CMSNs. (d, e) Tumor volume curves after the mice (n = 5) received different treatments. (e) Tumor volume and (f) tumor weight on the 14th day after different treatments (n = 5). (g) Pictures of tumors dissected on the 14th day after different treatments. (h) FDX1, DLAT, and BCAT1 staining of sliced tumors from different groups; scale bars = 100 μm. Intergroup comparison was performed using the *t*-test. [a]Not significant, [b]$p < 0.05$, and [c]$p < 0.0001$ (compared with the group I). (For interpretation of the references to color in this figure legend, the reader is referred to the Web version of this article.)

treatment, the mice were euthanized, and the tumors were collected. The tumors were photographed and weighed, and the results confirmed that XQ/Gp@CMSNs had the most significant antitumor effect *in vivo* (Fig. 6f and g). Hematoxylin–eosin (H&E) and TUNEL staining of the tumors indicated that, compared with PBS, all the formulations induced cell death in pancreatic cancer cells. Owing to the lack of tumor targeting by free gabapentin, the degree of cell death in Group II was the lowest. In contrast, owing to its excellent active targeting ability, XQ/Gp@CMSNs caused the largest area of cell death, and Ki-67 also had the lowest cell proliferation ability (Fig. S16). Tumor-associated fibroblasts (CAFs) highly express α-SMA. As extracellular matrix barriers, they play crucial roles in the growth, metastasis, and chemotherapy resistance of PDAC [60]. Immunohistochemical (IHC) results indicated that, compared with that in group I tumors, the expression level of α-SMA in tumors significantly decreased in group VI tumors, suggesting a potential reduction in the stromal barrier that contributes to drug resistance in PDAC. As a marker of endothelial cells, CD34 plays a significant role in tumor angiogenesis. Recent studies have demonstrated that a relatively high positive rate of CD34 is positively correlated with increased proliferative capacity and drug resistance in patients with PDAC [61]. In group VI, the downregulation of CD34 suggests an inhibitory effect on tumor angiogenesis, which could contribute to the observed antitumor efficacy by impairing nutrient and oxygen supply (Fig. S17). Compared with Group I and Group II, the copper-doped drug groups presented varying degrees of FDX1 and LIAS downregulation. DLAT oligomer formation resulted in the intense, punctate DLAT signal, which co-localizes with tumor cells in groups V and VI *in vivo*. The DLAT protein complexes are often unstable and may be degraded into smaller fragments during lysis and denaturation *in vitro*, as the western blot was performed under non-reducing conditions on homogeneous cell lysates. Consequently, the DLAT oligomerization was downregulated in the western blot. Owing to the inability of free gabapentin administered intravenously to effectively target tumor cells, the expression of BCAT1 in group II could not be fully inhibited. Nevertheless, nanoparticles containing gabapentin (groups IV and VI) benefit from the enhanced permeability and retention effect (EPR) effect and the active targeting capabilities of XQ-2d, thereby more effectively inhibiting BCAT1 expression. Mild downregulation of BCAT1 was also noted in the treatment group without gabapentin, potentially indicating a correlation with cell death induced by cuproptosis (Fig. 6h–S18).

2.11. Biosafety assessment

The changes in the body weights of the mice during the treatment period were closely monitored. Compared with those in Group I, the body weights of the mice in Groups III and VI slightly decreased ($p < 0.05$). However, no significant alterations in body weight were observed among Groups V and VI, indicating that the active targeting capability of XQ-2d effectively mitigated the systemic toxicity and side effects of the tumor-starvation therapy (Fig. S19a and b). After treatment, major organs (heart, liver, spleen, lungs, and kidneys) were collected from the mice across all the groups and stained with hematoxylin and eosin (H&E). Despite a mild reduction in body weight in Groups III and IV (lack of XQ-2d modification), no significant abnormalities were detected in the pathological results across all groups. These findings underscore the favorable biosafety profile of the developed nanodrug delivery system (Fig. S19c). Compared with those in Group I, further hematological examinations revealed increases in white blood cell and neutrophil counts within Group VI; however, no significant differences in other hematological indices were observed. This increase is presumed to be due to an inflammatory response, which is induced by significant necrosis of tumor cells because of the enhanced therapeutic efficacy demonstrated by Group VI (Fig. S19d–j). Biochemical analysis revealed decreased levels of albumin in groups III and IV, suggesting that non-XQ-2d-modified nanoparticles intervene in energy metabolism and have a more significant impact on nutritional status. Through the application of adapter modification, this concern has been effectively alleviated, indicating that the active targeting effect of XQ/Gp@CMSNs limits starvation therapy to the tumor site (Fig. S19k). Furthermore, the biochemical indices related to liver and kidney function did not significantly differ among the groups, which aligns with the observations from H&E staining pathological evaluations (Fig. S19c; l-o).

To quantitatively assess the potential risk of Cu accumulation and off-target toxicity, the Cu content in major organs was determined via ICP-MS after the 14-day treatment. The PEG/Gp@CMSNs treatment group demonstrated the highest Cu accumulation in the liver and spleen, indicating a higher potential for off-target toxicity. Nevertheless, although the XQ/Gp@CMSNs group also showed considerable Cu accumulation, the combined evidence from liver function indexes and organ H&E staining led us to conclude that this toxicity was controllable within the treatment course (Fig. S20).

2.12. Synergistic inhibitory effects of Cu^{2+} and gabapentin on tumors

We observed that DLAT is not only a critical protein associated with cuproptosis but also a key component of the pyruvate dehydrogenase complex (PDC), which catalyzes the decarboxylation of pyruvate to acetyl-CoA, thereby playing an essential role in the TCA cycle [26]. Given that the TCA cycle is downstream of BCAAs metabolism, we propose that Cu^{2+} and gabapentin synergistically inhibit tumor energy metabolism. To confirm this hypothesis, metabolomics analysis was performed on tumors. Compared with the PBS group, the XQ/Gp@CMSN group presented the upregulation of 135 metabolites and the downregulation of 37 metabolites (Fig. 7b). Furthermore, a KEGG pathway analysis was performed on the differentially abundant metabolites [62]. The horizontal axis represents the percentage of annotated differentially abundant metabolites in a certain pathway compared with all annotated differentially abundant metabolites, whereas the vertical axis represents the enriched KEGG metabolic pathway names. The results revealed significant differences in central carbon metabolism, primarily represented by the TCA cycle [63,64]. There are significant differences in amino acid metabolism, including BCAAs-related pathways (Fig. 7a–S21). This is attributed to the dual effects of Cu^{2+} and gabapentin. A comparison of differentially abundant metabolites among the groups was conducted to further elucidate the impact of gabapentin and Cu^{2+} on BCAAs metabolism. The results indicated that BCAAs were significantly different metabolites (VIP >1, $p < 0.05$). As shown in Fig. 7c–e, both gabapentin (Group II) and the CMSNs (Groups III and V) clearly elevated BCAAs levels, with a stronger effect observed when they were used in combination (Groups IV and VI). This change can be attributed to their combined inhibition of BCAAs metabolism and disruption of the TCA cycle. Notably, Groups V and VI presented even greater elevations in BCAAs levels, further confirming the active targeting capability conferred by XQ-2d modifications.

To further clarify the effects of gabapentin and Cu^{2+} on BCAAs metabolism, comparisons were made among the changes in the levels of BCKAs across different groups. The results, illustrated in Fig. 7f, indicate that gabapentin and CMSNs show a trend of downregulation and upregulation of BCKAs expression levels, respectively. This finding contrasts with the general upregulation observed in BCAAs levels, which can be attributed to their distinct mechanisms of action within BCAAs metabolism. Gabapentin exerts its influence by inhibiting BCAT 1, resulting in an increase in upstream BCAAs levels accompanied by a decrease in downstream BCAAs levels. In contrast, the inhibition of the downstream TCA cycle by PEG/CMSNs led to elevated concentrations of both BCAAs and BCKAs (Scheme 1). This effect was particularly pronounced within the XQ/CMSN group. Notably, when gabapentin was loaded (groups IV and VI), there was a marked decrease in the expression level of BCKA. These findings confirm that gabapentin and Cu^{2+} act on different targets in BCAAs metabolism and collectively exert synergistic inhibitory effects.

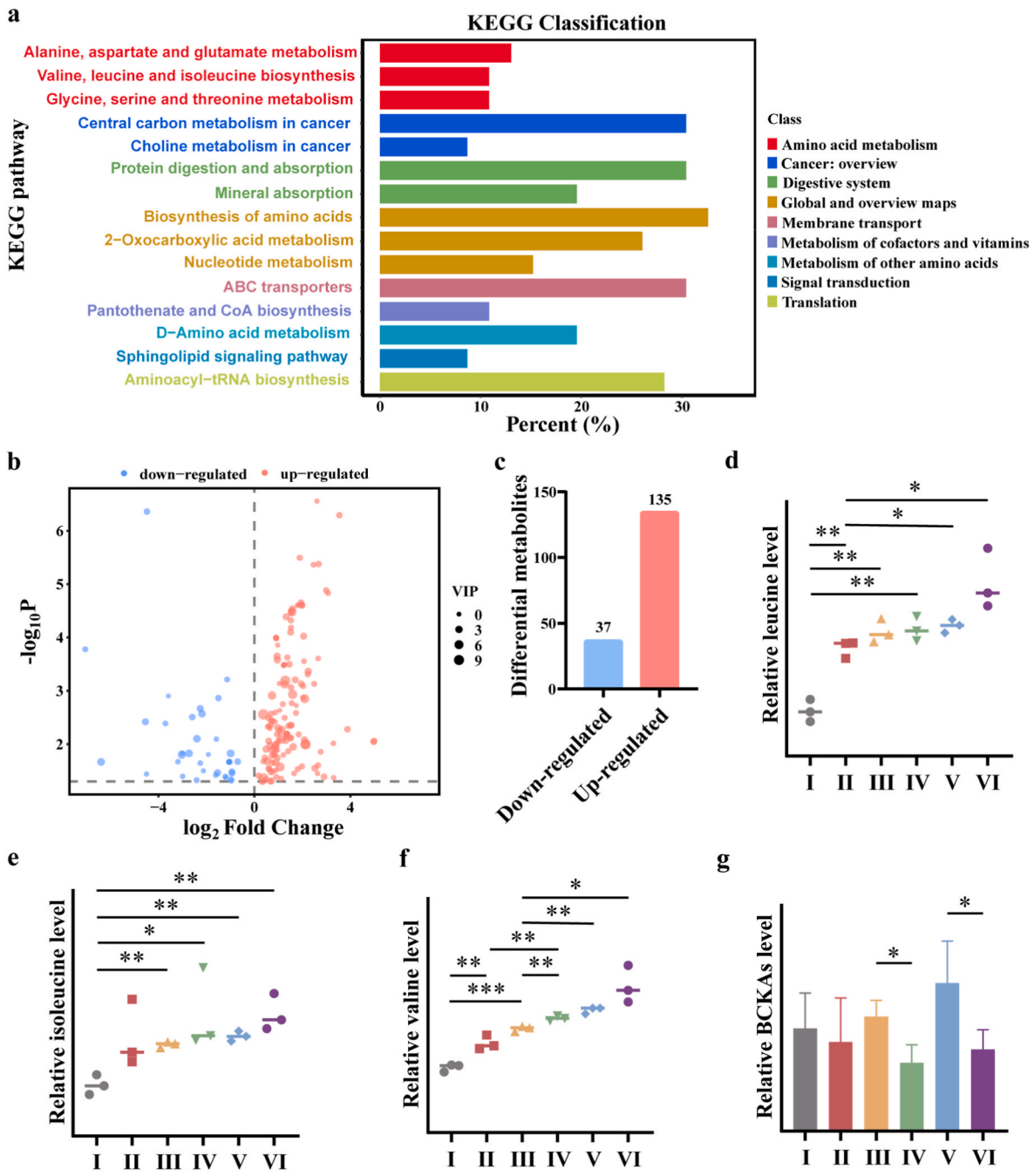

Fig. 7. Metabolomic analysis of tumors (I: PBS, II: Gp, III: PEG/CMSNs, IV: PEG/Gp@CMSNs, V: XQ/CMSNs, VI: XQ/Gp@CMSNs). (a) KEGG pathway analysis between groups I and VI. (b, c) Volcano plot of the differentially abundant metabolites between groups I and VI. (d–g) The expression levels of BCAAs and BCKAs in various groups. Intergroup comparison was performed using the *t*-test. $^{*}p < 0.05$, $^{**}p < 0.01$, and $^{***}p < 0.001$.

3. Conclusion

In summary, our research revealed that, compared with normal pancreatic tissue, PDAC tissue exhibits significant metabolic reprogramming of BCAAs. This reprogramming is associated with increased demand for BCAAs and other essential nutrients in tumors, which correlates with poorer patient outcomes. To address these metabolic alterations, we developed a novel therapeutic platform that enables acid-responsive release within the TME. This platform effectively selectively targets copper ions and BCAAs to enhance copper-induced cell death and starvation therapy, thereby effectively inhibiting the malignant proliferation of pancreatic cancer cells. The inclusion of gabapentin serves as a potent inhibitor of BCAT1, disrupting BCAAs metabolism and consequently impairing the energy supply to cancer cells. Under the acidic and high H_2O_2 conditions typical of the TME, the released Cu^{2+} ions synergistically promote oxidative damage through Fenton-like reactions, further enhancing the therapeutic effects of gabapentin. This dual mechanism leads to cuproptosis and disrupts the TCA cycle, ultimately contributing to the observed cytotoxicity. Both *in vitro* and *in vivo* experiments confirmed the strong cytotoxic effects of XQ/Gp@CMSNs, with metabolomic analyses elucidating the underlying therapeutic mechanisms. Compared with gabapentin alone and unmodified nanoparticles, XQ/Gp@CMSNs demonstrated significantly improved efficacy and retention time within tumors. Given their favorable biosafety profile, XQ/Gp@CMSNs represent a promising advancement in tumor-starvation therapies, addressing critical challenges associated with

side effects and limited chemotherapy regimens for patients with pancreatic cancer. The development of XQ/Gp@CMSNs opens new avenues for research into targeted metabolic interventions in pancreatic cancer. However, the subcutaneous tumor model cannot fully recapitulate the complex microenvironment of human pancreatic cancer; more clinically relevant orthotopic models would be prioritized for validation in future studies. Furthermore, efforts should focus on optimizing the formulation to enhance targeting and release kinetics, as well as on exploring combination therapies that leverage PDAC's metabolic vulnerabilities. Ultimately, our findings underscore the importance of metabolic reprogramming in cancer therapy and the potential of innovative nanomedicine approaches to improve patient outcomes for this aggressive disease.

4. Experimental section

4.1. Subjects

Approval was obtained from the Ethics Committee of Fujian Medical University Union Hospital (No. 2014007; 2020WSJK037), with all procedures adhering to the 1964 Declaration of Helsinki and its subsequent amendments or comparable ethical standards. A total of 115 participants with PDAC were recruited from patients admitted to Fujian Medical University Union Hospital. The diagnosis of PDAC in these patients was confirmed through surgical specimens. Patients with severe liver, kidney, or endocrine disorders were excluded. The tumor samples were collected during surgery, yielding a total of 91 PDAC samples and 24 pairs of cancerous and adjacent noncancerous samples. Collect demographic information of patients.

4.2. Metabolomic analysis of clinical tumor samples

Metabolite extraction The tumor samples were collected and combined with beads and 500 μL of extraction solution composed of MeOH, ACN, and H_2O at a 2:2:1 vol ratio, which also included deuterated internal standards. The mixture was vortexed for 30 s. Subsequently, the samples were homogenized at 35 Hz for 4 min and sonicated in a 4 °C water bath for 5 min; this process was repeated three times. The samples were then incubated at −40 °C for 1 h to precipitate the proteins. Following incubation, the samples were centrifuged at 12000 rpm for 15 min at 4 °C. The supernatant was transferred to a new glass vial for analysis. A quality control (QC) sample was prepared by mixing equal volumes of the supernatants from the samples.

LC−MS/MS analysis LC−MS/MS analyses of polar metabolites were conducted via a UHPLC system (Vanquish, Thermo Fisher Scientific) interfaced with a Waters ACQUITY UPLC BEH Amide column (2.1 mm × 50 mm, 1.7 μm) and an Orbitrap Exploris 120 mass spectrometer (Orbitrap MS, Thermo). The mobile phase was composed of 25 mmol/L ammonium acetate and 25 mmol/L ammonia hydroxide in water at pH 9.75 (A) and acetonitrile (B). The autosampler was maintained at 4 °C, and the injection volume was set to 2 μL. The Orbitrap Exploris 120 instrument was operated in information-dependent acquisition (IDA) mode controlled by acquisition software (Xcalibur, Thermo), which continuously assesses the full-scan MS spectrum. The parameters for the ESI source were set as follows: the sheath gas flow rate was 50 arbitrary units (Arb), the auxiliary gas flow rate was 15 Arb, the capillary temperature was maintained at 320 °C, the full MS resolution was 60,000, and the MS/MS resolution was 15,000. The stepped normalized collision energy (SNCE) was plotted to 20/30/40, and the spray voltage was applied at either +3.8 kV (positive mode) or −3.4 kV (negative mode).

Metabolomics Data Analysis The preprocessed data were subjected to multivariate statistical analysis via SIMCA (V18.0.1, Sartorius Stedim Data Analytics AB, Umea, Sweden), with UV scaling applied. Initially, principal component analysis (PCA) and orthogonal partial least squares discriminant analysis (OPLS-DA) were conducted to obtain VIP values for differentially abundant metabolites. Additionally, a permutation test with 200 permutations was performed to assess potential overfitting. The differentially abundant metabolites were selected on the basis of the VIP value and P values, with VIP >1 and $P < 0.05$ serving as the criteria for identifying these metabolites.

To evaluate the variability in the metabolome of PDAC, the samples were categorized into subgroups via hierarchical cluster analysis (HCA). This categorization was determined by the relative metabolite content, which was calculated on the basis of the area beneath the characteristic peak of each metabolite. Hierarchical clustering employs a bottom-up agglomerative approach, where each sample begins as an individual cluster. In each subsequent step, the most similar clusters were merged until all were consolidated into a single cluster. The Euclidean distance metric was applied to measure the distance between pairs of samples, whereas Ward's method was utilized to determine the distance between clusters [65]. The entire cluster analysis was conducted via the MetaboAnalyst 5.0 online platform. The 91 PDAC patients were subsequently divided into high- and low-BCAAs groups on the basis of the concentration of BCAAs.

Survival analysis The Kaplan−Meier (K−M) curve was used to estimate the survival time of patients with PDAC in the high- and low-BCAAs groups. This nonparametric estimation method for survival analysis addresses the issue of right censoring, a common challenge in survival studies. Additionally, the K−M curve provides a visual representation of survival rates or mortality across two or more groups, thereby enabling the identification of differences in long-term prognosis among patients belonging to different metabolic types through survival analysis.

4.3. Materials Required for drug delivery experiments

Tetraethyl orthosilicate (TEOS), hexadecyl trimethyl ammonium bromide (CTAB), ammonia solution ($NH_3{\cdot}H_2O$), ethanol, copper nitrate trihydrate (Cu $[NO_3]_2{\cdot}3H_2O$), hydrochloric acid (HCl) and sodium hydroxide (NaOH) were obtained from Sinopharm Chemical Reagent Co. (Shanghai, China). Mal-PEG2000-silane was purchased from AVT Pharmaceutical Technology Co., Ltd. (Shanghai, China). Gabapentin was obtained from Aladdin Biochemical Technology Co. (Shanghai, China). PATU-8988 and BxPC-3 cells were acquired from MeisenCTCC Cell Technology Co., Ltd. (Zhejiang, China). A Cell Counting Kit-8 (CCK-8), an Annexin V-FITC/PI kit, calcein-AM and propidium iodide (PI), a JC-1 Mitochondrial Membrane Potential Assay Kit, Cell Mitochondria Isolation Kit, and 2′,7′-dichlorofluorescin diacetate (DCFH-DA) were purchased from Beyotime Biotechnology Co. (Haimen, China). Phosphate-buffered saline (PBS) was acquired from Herui Biotechnology (Fujian, China). Simulated Body Fluid (SBF) was acquired from Solarbio Science & Technology (Beijing, China). GAPDH antibody was purchased from Bioss (Beijing, China). All other antibodies (dihydrolipoamide S-acetyltransferase (DLAT), ferredoxin-1 (FDX1), lipoyl synthase (LIAS) and branched chain aminotransferase 1 (BCAT1)) were purchased from Sanying Biology Technology Co. (Wuhan, China). Cy3-decorated XQ-2d-SH and XQ-2d-SH were obtained from Sangon Biotech (Shanghai, China).

4.4. Preparation of mesoporous silica nanoparticles (MSNs)

The synthesis of MSNs was improved on the basis of the Stöber method [43,66]. Briefly, 0.50 g of CTAB and 3.5 mL of NaOH (1 M) were dissolved in 240 mL of H_2O. At 80 °C, 2.50 mL of TEOS was slowly added to the solution at 80 °C while stirring until a white precipitate was obtained. The mixture was subsequently centrifuged at 12,000 rpm for 20 min to remove the supernatant. The precipitate was washed three times with water and ethanol to obtain the MSNs.

4.5. Preparation of targeted copper-doped MSNs loaded with gabapentin (XQ/Gp@CMSNs)

First, copper-doped MSNs (CMSNs) were synthesized via a hydrothermal method. Briefly, 40 mg of preformed MSNs and 104 mg of Cu $(NO_3)_2{\cdot}3H_2O$ were added to 36 mL of H_2O. Subsequently, 4 mL of 30 % $NH_3{\cdot}H_2O$ was added under ultrasonication. After thorough mixing, the solution was transferred to a 50 mL Teflon liner in a stainless-steel chamber and reacted at 140 °C for 10 h. The product was then centrifuged at 14,000 rpm for 20 min and washed three times with ethanol. The ethanol suspension of the product was then subjected to rotary evaporation at 60 °C to obtain the CMSN powder.

To achieve targeted drug delivery, we modified CMSNs with XQ-2d (XQ/CMSNs) via our previously reported protocol [36]. Initially, the CMSNs were PEGylated to increase their hydrophilicity and biocompatibility. Specifically, 5 mg of CMSNs and 25 mg of MAL-PEG2000-silane were dispersed in 50 mL of ethanol and stirred at 60 °C for 24 h. After cooling to room temperature, the precipitate was washed and then stirred with XQ-2d-HS (100 mM, 100 μL) at 4 °C for 12 h. Following washing with TM buffer, the product was collected by centrifugation, yielding the final XQ/CMSNs.

To obtain the final drug loaded with gabapentin, 10 mg XQ/CMSNs were dispersed in gabapentin solution (20 mg/mL, 1 mL) and stirred at 4 °C for 8 h. After centrifugation (18,000 rpm, 5 min), XQ/Gp@CMSNs were obtained, and the concentration of gabapentin in the supernatant was measured via high-performance liquid chromatography (HPLC). The loading rate was calculated.

4.6. Characterization

TEM images and energy dispersive X-ray spectroscopy (EDS) data were obtained on a Talos F200S instrument (Thermo Fisher Scientific, Waltham, MA, USA). SEM images of the morphology of the CMSNs were acquired with a GeminiSEM 300 (Zeiss, Oberkochen, Germany). The hydrodynamic particle sizes of the samples were determined via DLS on a Litesizer DLS 500 (Anton Paar Graz, Austria). The content of each element was quantified via XRD (Rigaku SmartLab SE, Rigaku, Tokyo, Japan; 2θ ranging from 10° to 80° Cu Kα1), and the synthesized nanoparticles were subjected to phase analysis. The valence states of the elements in the CMSNs were analyzed via XPS (Thermo Fisher Scientific, Waltham, MA, USA), the C_{1s} peak of carbon (284.8 eV) is used for data calibration. FTIR spectra were measured via a Bruker Vector 22 spectrometer (Billerica, MA, USA). UV–vis absorption spectra were recorded on a UV-2600 spectrometer (Shimadzu, Kyoto, Japan). Nitrogen (N_2) adsorption−desorption isothermal curves and the corresponding pore size distributions of the MSNs and CMSNs were assessed via an ASAP 2460 (Micromeritics, Norcross, GA, USA). CLSM images were acquired on a TCS SP8 CLSM (Leica, Wetzlar, Germany). For the cell migration experiments, the cells were observed with a Leica DMI3000 B (Leica, Wetzlar, Germany). Flow cytometric analysis was performed on a BD FACSCanto II flow cytometer (Becton Dickinson, Franklin Lakes, NJ, USA). The Cu and Si contents were quantitatively analyzed via ICP−MS (Agilent 7800, Santa Clara, CA, USA), whereas the gabapentin content was determined via HPLC (Thermo Fisher Scientific, Waltham, MA, USA). The detection of CCK-8 and ·OH was conducted via a Multiska FC microplate reader (Thermo Fisher Scientific, Waltham, MA, USA). The ESR spectrum were measured via a Bruker EMXplus-6/1 (Billerica, MA, USA).

4.7. Release of XQ/Gp@CMSNs at different pH values

To evaluate the degradation of XQ/Gp@CMSNs at different pH values, 10 mg of XQ/Gp@CMSNs were dispersed in 20 mL of PBS at pH 7.4 and pH 6.5. After stirring at 37 °C, 1 mL of sample was extracted after 1, 2, 4, 6, 8, 10, 12, and 24 h. The concentrations of Cu and gabapentin in the solution were determined via ICP−MS or HPLC. Additionally, TEM images were obtained at 0, 12, and 24 h to observe changes in the morphology of the samples. Parallel experiments were conducted in SBF at different pH values to determine the concentrations of Cu and Si at corresponding time points.

4.8. XQ/Gp@CMSNs generate ·OH through a Fenton-like reaction

TMB (40 μg/mL) was mixed with XQ/Gp@CMSNs (1 mg) and H_2O_2 (1 mM) at pH 7.4 and pH 6.5, respectively, and incubated at 37 °C for 30 min. The absorbance at 650 nm was measured. The experiment was repeated with 1 mmol/L Cu^{2+} replacing XQ/Gp@CMSNs. TMB solutions treated with Cu^{2+} or H_2O_2 alone were used as control groups.

4.9. Detection of intracellular ROS generation

PATU-8988 and BxPC-3 cells were incubated in CLSM-exclusive culture dishes to allow them to adhere to the surface. They were then incubated for 24 h in culture media containing the same drug concentrations (CMSNs 30 μg/mL): fresh DMEM/RPMI-1640, PEG/MSNs, gabapentin, PEG/CMSNs, PEG/Gp@CMSNs, XQ/CMSNs, and XQ/Gp@CMSNs. After incubation, the DCFH-DA probe (10 μM) was added, and the cells were incubated for an additional 20 min. Subsequently, the cells were washed three times with serum-free medium. The fluorescence intensity was observed via CLSM at an excitation wavelength of 488 nm, which represents the generation of ROS.

4.10. Cellular internalization and organelle localization of XQ/CMSNs

***In vitro* cell internalization** Cy3 was used to label nanoparticles to verify the targeting ability of XQ/CMSNs. $PEG/CMSNs^{Cy3}$ and $XQ/CMSNs^{Cy3}$ were co-cultured with pancreatic cancer cells for 3 or 6 h. The differences in fluorescence intensity among the groups were observed using CLSM and quantitative analysis was performed.

Determination of mitochondrial copper content PEG/CMSNs and XQ/CMSNs (CMSNs: 30 μg/mL)were co-incubated with pancreatic cancer cells for different periods of time. The cell mitochondria were isolated using a Cell Mitochondria Isolation Kit, and the copper content in the mitochondria was determined by ICP-MS.

4.11. In vitro cytotoxicity experiments

CCK-8 Assay Cell viability was assessed via the CCK-8 assay. In a typical experiment, PATU-8988 or BxPC-3 cells were cultured in 96-well plates and treated with corresponding concentrations of MSNs, gabapentin, PEG/CMSNs, PEG/Gp@CMSNs, XQ/CMSNs, or XQ/Gp@CMSNs. After 48 h, the cells were washed with PBS, and the medium in each well was replaced with 10 % CCK-8. After incubation at 37 °C for 4 h, the absorbance at 450 nm was measured. Using AC16 cells to evaluate the cytotoxicity of XQ/Gp@CMSNs under the same conditions.

Calcein AM/PI Staining To observe live and dead cells via an inverted fluorescence microscope, PATU-8988/BxPC-3 cells were seeded in 96-well plates overnight. After being incubated with DMEM/RPMI-1640, MSNs, gabapentin, PEG/CMSNs, PEG/Gp@CMSNs, XQ/CMSNs, or XQ/Gp@CMSNs for 48 h, the cells were processed via the Calcein/PI Assay Kit and observed under an inverted fluorescence microscope. Live cells presented green fluorescence (λ_{ex} = 494 nm, λ_{em} = 517 nm), whereas dead cells presented red fluorescence (λ_{ex} = 535 nm, λ_{em} = 617 nm).

Cell Migration Experiments Cell migration was observed under a microscope. PATU-8988 or BxPC-3 cells were seeded in 6-well plates and allowed to reach confluence. After a scratch wound was created, the corresponding formulations were added, and the samples were incubated in an incubator. Cell migration was observed under a microscope at 0, 12, and 24 h posttreatment.

Flow cytometric analysis of apoptosis Apoptosis was analyzed via

FITC/PI double staining. PUA8988 or BxPC-3 cells were seeded in 6-well plates and allowed to adhere. After the cells were incubated for 48 h with the corresponding formulation, they were digested, and the cells were collected via trypsin. The cells were washed and resuspended twice with PBS. Next, 195 μL of Annexin V-FITC binding buffer, 5 μL of Annexin V-FITC, and 10 μL of PI were added, after which the mixture was resuspended and mixed thoroughly. The mixture was incubated in the dark at 25 °C for 20 min, after which it was detected via a flow cytometer.

4.12. Mitochondrial function detection

To evaluate the impact of drugs on mitochondrial function. The Mitochondrial Membrane Potential Assay Kit with JC-1 was used for detection, and PATU-8988 or BxPC-3 cells were evenly seeded in 6-well plates with 1 mL of medium per well. After the cells were incubated with the corresponding formulation for 48 h, they were collected via trypsin. The cells were resuspended in 0.5 mL of culture medium mixed with 0.5 mL of JC-1 working solution and incubated for 20 min. The cells were washed with JC-1 buffer solution and resuspended. Finally, the cells were detected via a flow cytometer.

4.13. In vivo tumor therapy

The animal experiment section has been approved by the Ethics Committee of Fujian Medical University (No.: IACUC FJMU 2024-0132). To evaluate therapeutic efficacy *in vivo*, male BALB/C nude mice were randomly divided into six groups (n = 5), and a xenograft tumor model was established via the subcutaneous injection of PATU-8988 cells (5×10^6 cells per mouse). When the tumor size reached 100 mm^3, the mice were administered PBS containing the corresponding formulations (100 μL) via tail vein injection. The control group mice were administered only PBS. The formulations were administered every 3 days, and tumor size and body weight changes were recorded every other day. After 14 days, the mice were euthanized, and their tumors were sectioned and analyzed via H&E staining, IHC, and immunofluorescence (IF). The hearts, livers, spleens, kidneys, and lungs were also harvested for H&E staining.

4.14. Biodistribution

After the xenograft tumor models were successfully established, the mice were randomly divided into two groups and injected with PEG/CMSNs or XQ/CMSNs labeled with Cy5.5 via the tail vein. The fluorescence distribution in the mice was monitored via the IVIS Spectrum system (PerkinElmer, Waltham, MA, USA) at 0, 6, 12, 24, and 36 h postinjection. After that, the major organs, including the heart, liver, spleen, lungs, kidneys, and tumors, were harvested from the mice. After washing with physiological saline, the organs were observed for fluorescence signals via the IVIS Spectrum. Organs were sampled and their Cu contents were performed by measuring through ICP-MS.

4.15. Metabolomic analysis of the xenograft tumor model

The methods of metabolite extraction, LC−MS/MS analysis and differentially abundant metabolite screening were the same as previously described. After that, the expression levels of BCAAs and BCKAs from the differentially abundant metabolites obtained with VIP >1 and $P < 0.05$ as the criteria were determined.

Metabolic Pathway Analysis MetaboAnalyst 5.0 (http://www.metaboanalyst.ca) combined with the KEGG database (https://www.kegg.jp/kegg/pathway.html) was used for pathway analysis on the basis of the screened differentially abundant metabolites. The criteria for identifying a pathway as sufficiently impacted across different groups were set as an "impact" value greater than 0.1 and a minimum of 2 ″hits" [62,67]. On the basis of the functional information of genes and genomes and guided by metabolic reactions, we connected possible metabolic pathways and their corresponding regulatory proteins. This is illustrated in a graphical manner to showcase cellular physiological and biochemical processes, along with conserved subpathways within the same lineage. Additionally, we organized all pathways that map differentially abundant metabolites of *Mus musculus* (mouse).

CRediT authorship contribution statement

Han Shi: Writing – original draft, Software, Methodology, Formal analysis, Data curation, Conceptualization. **Zhiqiang Xie:** Validation, Data curation. **Junrong Zhang:** Writing – review & editing, Methodology. **Fengchun Lu:** Writing – review & editing, Resources. **Haoteng Luo:** Writing – review & editing, Data curation. **Pengfei Guo:** Software, Formal analysis, Data curation. **Meichen Jiang:** Methodology. **Zongqi Weng:** Data curation. **Xin Luo:** Data curation. **Bing Chen:** Writing – review & editing, Methodology, Funding acquisition. **Heguang Huang:** Writing – review & editing, Resources, Funding acquisition. **Tianhong Teng:** Writing – review & editing, Project administration, Methodology, Funding acquisition.

Informed consent

Informed consent forms were signed by all participating patients.

Ethical approval

The study was approved by the ethical committees of Fujian Medical University (No. IACUC FJMU 2024–0132) and Fujian Medical University Union Hospital (No. 2014007; 2020WSJK037). All methods were performed in accordance with the relevant guidelines and regulations.

Declaration of competing interest

The authors declare that they have no known competing financial interests or personal relationships that could have appeared to influence the work reported in this paper.

Acknowledgments

This work was supported by the National Natural Science Foundation of China, Grant/Award Number: 82103689; Excellent Young Scholars Cultivation Project of Fujian Medical University Union Hospital, Grant/Award Number: 2022XH028/2022XH049; Natural Science Foundation of Fujian Province, China, Grant/Award Number: 2025J01764 and 2024J01505; Joint Funds for the Innovation of Science and Technology, Grant/Award Number: 2024Y9286. The authors extend their gratitude to Prof. Tan from Hangzhou Institute of Medicine (HIM) for providing the nucleotide sequence of the aptamer. The authors extend their gratitude to Mr. He from the Shiyanjia Laboratory (www.shiyanjia.com) for providing invaluable assistance with the TEM analysis. The authors acknowledge the Fujian Medical University Ethics Committee for their kind guidance in the animal experiments and extend their sincere thanks to the Public Technology Service Center of Fujian Medical University, in particular to Mr. Lin Junjin, Ms. Yan Cailing, and Ms. Zheng Shuping, for their technical support and assistance. The authors thank Kanehisa Laboratories for granting permission to use the metabolic pathway image.

Appendix A. Supplementary data

Supplementary data to this article can be found online at https://doi.org/10.1016/j.mtbio.2025.102477.

Data availability

Data will be made available on request.

References

[1] R.L. Siegel, et al., Cancer statistics, 2025, CA Cancer J. Clin. 75 (1) (2025) 10–45.
[2] D. Wu, et al., 3D printing-biomimetic local stiff niche enhances glycolysis to boost PDAC cell stem-like phenotype via N6-methyladenosine-suppressed YAP1 mRNA decay, Mater. Today Bio 34 (2025) 102176.
[3] M. Yin, Q.Y. Lei, BCAT2-BCKDH metabolon maintains BCAA homeostasis, Nat. Metab. 4 (12) (2022) 1618–1619.
[4] L. Qian, et al., Enhanced BCAT1 activity and BCAA metabolism promotes RhoC activity in cancer progression, Nat. Metab. 5 (7) (2023) 1159–1173.
[5] D. Yang, et al., Branched-chain amino acid catabolism breaks glutamine addiction to sustain hepatocellular carcinoma progression, Cell Rep. 41 (8) (2022) 111691.
[6] X. Wu, et al., NIR-II imaging-guided precise photodynamic therapy for augmenting tumor-starvation therapy by glucose metabolism reprogramming interference, Sci Bull (Beijing) 69 (9) (2024) 1263–1274.
[7] X. Wang, et al., Molecular mechanism and pharmacokinetics of flavonoids in the treatment of resistant EGF receptor-mutated non-small-cell lung cancer: a narrative review, Br. J. Pharmacol. 178 (6) (2021) 1388–1406.
[8] S.R. Stockwell, et al., Selective Aurora A-TPX2 interaction inhibitors have in vivo efficacy as targeted antimitotic agents, J. Med. Chem. 67 (17) (2024) 15521–15536.
[9] W. Sun, et al., Synergistic ROS/enzyme dual-responsive oral drug delivery system: a novel multi-mechanistic platform for spatiotemporal control and overcoming drug resistance in colorectal cancer therapy, Mater. Today Bio 33 (2025) 101920.
[10] Q. Lin, et al., Design and application of pH-Responsive liposomes for site-specific delivery of cytotoxin from Cobra venom, Int J Nanomedicine 19 (2024) 5381–5395.
[11] M. Go, et al., BCAT1 promotes osteoclast maturation by regulating branched-chain amino acid metabolism, Exp. Mol. Med. 54 (6) (2022) 825–833.
[12] Q. Liao, et al., Novel insights into histone lysine methyltransferases in cancer therapy: from epigenetic regulation to selective drugs, J. Pharm. Anal. 13 (2) (2023) 127–141.
[13] D. Oktyabri, et al., DOT1L histone methyltransferase regulates the expression of BCAT1 and is involved in sphere formation and cell migration of breast cancer cell lines, Biochimie 123 (2016) 20–31.
[14] W. Zhu, Y. Shao, Y. Peng, MicroRNA-218 inhibits tumor growth and increases chemosensitivity to CDDP treatment by targeting BCAT1 in prostate cancer, Mol. Carcinog. 56 (6) (2017) 1570–1577.
[15] X. Guo, et al., BCAA insufficiency leads to premature ovarian insufficiency via ceramide-induced elevation of ROS, EMBO Mol. Med. 15 (4) (2023) e17450.
[16] N. Ueda, A rheostat of ceramide and Sphingosine-1-Phosphate as a determinant of oxidative stress-mediated kidney injury, Int. J. Mol. Sci. 23 (7) (2022).
[17] S. Ding, et al., Curcumin-loaded nanoscale coordination polymers for ROS scavenging and anti-inflammatory therapy in atherosclerosis, Mater. Today Bio 34 (2025) 102152.
[18] J.B. Spinelli, M.C. Haigis, The multifaceted contributions of mitochondria to cellular metabolism, Nat. Cell Biol. 20 (7) (2018) 745–754.
[19] H. Peng, et al., Unraveling mitochondria-targeting reactive oxygen species modulation and their implementations in cancer therapy by nanomaterials, Exploration (Beijing) 3 (2) (2023) 20220115.
[20] C. Zheng, et al., Dynamic regulation of drug biodistribution by turning tumors into decoys for biomimetic nanoplatform to enhance the chemotherapeutic efficacy of breast cancer with bone metastasis, Exploration (Beijing) 3 (4) (2023) 20220124.
[21] L. Wang, et al., A multifunctional self-assembled hydrogel with bactericidal activity and macrophage metabolic reprogramming for diabetic bone defect repair, Mater. Today Bio 34 (2025) 102162.
[22] B. Guo, et al., Cuproptosis induced by ROS responsive nanoparticles with Elesclomol and copper combined with αPD-L1 for enhanced cancer immunotherapy, Adv Mater 35 (22) (2023) e2212267.
[23] J. Li, et al., Engineered anti-cancer nanomedicine for synergistic cuproptosis-immunotherapy, Mater. Today Bio 34 (2025) 102133.
[24] D. Tang, G. Kroemer, R. Kang, Targeting cuproplasia and cuproptosis in cancer, Nat. Rev. Clin. Oncol. 21 (5) (2024) 370–388.
[25] Q. Xue, et al., Copper metabolism in cell death and autophagy, Autophagy 19 (8) (2023) 2175–2195.
[26] P. Tsvetkov, et al., Copper induces cell death by targeting lipoylated TCA cycle proteins, Science 375 (6586) (2022) 1254–1261.
[27] Y. Liu, et al., Single-Site nanozymes with a highly conjugated coordination structure for antitumor immunotherapy via cuproptosis and cascade-enhanced T lymphocyte activity, J. Am. Chem. Soc. 146 (6) (2024) 3675–3688.
[28] L. Wang, et al., Targeted delivery of CEBPA-saRNA for the treatment of pancreatic ductal adenocarcinoma by transferrin receptor aptamer decorated tetrahedral framework nucleic acid, J Nanobiotechnology 22 (1) (2024) 392.
[29] C. Wang, et al., Ferritin-based targeted delivery of arsenic to diverse leukaemia types confers strong anti-leukaemia therapeutic effects, Nat. Nanotechnol. 16 (12) (2021) 1413–1423.
[30] Q. Yang, et al., Regulating the properties of XQ-2d for targeted delivery of therapeutic agents to pancreatic cancers, Natl. Sci. Rev. 10 (8) (2023) nwad113.
[31] C. Zhu, et al., Recent progress of SELEX methods for screening nucleic acid aptamers, Talanta 266 (Pt 1) (2024) 124998.
[32] B. Chen, et al., B7H3 targeting gold nanocage pH-sensitive conjugates for precise and synergistic chemo-photothermal therapy against NSCLC, J Nanobiotechnology 21 (1) (2023) 378.
[33] Z. Xue, et al., The nucleic acid reactions on the nanomaterials surface for biomedicine, J Nanobiotechnology 23 (1) (2025) 308.
[34] Y. Liao, et al., The research advances of aptamers in hematologic malignancies, Cancers (Basel) 15 (1) (2023) 300.
[35] X. Wu, et al., Elucidation and structural modeling of CD71 as a molecular target for cell-specific aptamer binding, J. Am. Chem. Soc. 141 (27) (2019) 10760–10769.
[36] D. Zhang, et al., Nanoparticles for near-infrared light-driven singlet oxygen and CO gas cogeneration for pancreatic adenocarcinoma therapy, ACS Appl. Nano Mater. 5 (11) (2022) 16741–16752.
[37] W. Xu, et al., Hollow Calcium/Copper bimetallic amplifier for Cuproptosis/Paraptosis/Apoptosis cancer therapy via Cascade reinforcement of endoplasmic reticulum stress and mitochondrial dysfunction, ACS Nano 18 (43) (2024) 30053–30068.
[38] W. Xu, et al., Tumor microenvironment responsive hollow nanoplatform for triple amplification of oxidative stress to enhance Cuproptosis-Based synergistic cancer therapy, Adv Healthc Mater 12 (13) (2023) 2202949.
[39] W. Zhang, et al., A peptide-copper self-assembled nanoparticle for enhanced cuproptosis by metabolic reprogramming in tumor cells, ACS Nano 18 (50) (2024) 34244–34256.
[40] S. Theivendran, S. Lazarev, C. Yu, Mesoporous silica/organosilica nanoparticles for cancer immunotherapy, Exploration (Beijing) 3 (3) (2023) 20220086.
[41] J.-E. Cun, et al., Copper-based bio-coordination nanoparticle for enhanced pyroptosis-cuproptosis cancer immunotherapy through redox modulation and glycolysis inhibition, Small 21 (6) (2025) 2409875.
[42] L. Qian, et al., Enhanced BCAT1 activity and BCAA metabolism promotes RhoC activity in cancer progression, Nat. Metab. 5 (7) (2023) 1159–1173.
[43] Z.A. Chen, et al., Receptor ligand-free mesoporous Silica nanoparticles: a streamlined strategy for targeted drug delivery across the blood-brain barrier, ACS Nano 18 (20) (2024) 12716–12736.
[44] S.G. Hong, T.C. Wang, Effect of copper oxides on the thermal oxidative degradation of the epoxy resin, J. Appl. Polym. Sci. 52 (9) (2003) 1339–1351.
[45] Y. Lu, et al., Chrono-controlled hydrogel platform orchestrates metabolic reprogramming and cuproptosis-driven immune activation against triple-negative breast cancer, Biomaterials 325 (2025) 123568.
[46] H.-F. Lu, et al., A highly selective and sensitive colorimetric uric acid biosensor based on Cu(II)-catalyzed oxidation of 3,3′,5,5′-tetramethylbenzidine, Sensor Actuat B-Chemical 244 (2017) 77–83.
[47] Q. Pan, et al., Two birds with one stone: copper metal-organic framework as a carrier of disulfiram prodrug for cancer therapy, Int J Pharmaceut 612 (2022) 121351.
[48] H. Li, et al., Engineering superstable islets-laden chitosan microgels with carboxymethyl cellulose coating for long-term blood glucose regulation in vivo, Carbohydr. Polym. 323 (2024) 121425.
[49] C. von Baeckmann, et al., On the importance of the linking chemistry for the PEGylation of mesoporous silica nanoparticles, J. Colloid Interface Sci. 589 (2021) 453–461.
[50] B. He, et al., Covalent organic frameworks interfacial modification of ceramic electrolytes for enhanced electrochemical performance, Adv. Funct. Mater. 35 (10) (2024) 2416779.
[51] C. Li, X. Chen, J. Zhang, Comment on: "development of a CLDN18.2-targeting immuno-PET probe for non-invasive imaging in gastrointestinal tumors", J. Pharm. Anal. 13 (9) (2023) 958–959.
[52] B. Zhao, et al., Multidrug resistance genes screening of pancreatic ductal adenocarcinoma based on sensitivity profile to chemotherapeutic drugs, Cancer Cell Int. 22 (1) (2022) 374.
[53] B.J. Aubrey, et al., How does p53 induce apoptosis and how does this relate to p53-mediated tumour suppression? Cell Death Differ. 25 (1) (2018) 104–113.
[54] T. Li, et al., Copper-coordinated covalent organic framework produced a robust fenton-like effect inducing immunogenic cell death of tumors, Macromol. Rapid Commun. 44 (11) (2023) e2200929.
[55] A. Perelman, et al., JC-1: alternative excitation wavelengths facilitate mitochondrial membrane potential cytometry, Cell Death Dis. 3 (11) (2012) e430.
[56] J. Zhong, et al., Inducing pyroptosis and cuproptosis using copper carriers for ROS-Augmented effective cancer therapy, ACS Materials Lett 6 (9) (2024) 4282–4290.
[57] J. Li, et al., Prognostic value and immune infiltration analyses of cuproptosis-related genes in hepatocellular carcinoma, Acta Materia Medica 2 (4) (2023).
[58] W. Mao, et al., Cuproptosis-related MTF1 inhibits kidney renal clear cell carcinoma progression by suppressing proliferation and regulating immune cell infiltration, Acta Materia Medica 2 (3) (2023) 310–322.
[59] M. Mu, et al., Boosting ferroptosis and microtubule inhibition for antitumor therapy via a carrier-free supermolecule nanoreactor, J. Pharm. Anal. 13 (1) (2023) 99–109.
[60] X. Chen, E. Song, Turning foes to friends: targeting cancer-associated fibroblasts, Nat. Rev. Drug Discov. 18 (2) (2019) 99–115.
[61] Z. Shah, et al., Human anti-PSCA CAR macrophages possess potent antitumor activity against pancreatic cancer, Cell Stem Cell 31 (6) (2024) 803–817 e6.
[62] M. Kanehisa, et al., KEGG for taxonomy-based analysis of pathways and genomes, Nucleic Acids Res. 51 (D1) (2023) D587–d592.
[63] G. Su, et al., Enteric coronavirus PDCoV evokes a non-warburg effect by hijacking pyruvic acid as a metabolic hub, Redox Biol. 71 (2024) 103112.
[64] W. Wu, et al., In situ diversity of metabolism and carbon use efficiency among soil bacteria, Sci. Adv. 8 (44) (2022) eabq3958.

[65] J.H. Ward, Hierarchical grouping to optimize an objective function, J. Am. Stat. Assoc. 58 (301) (1963) 236–244.
[66] Y. Huang, et al., Reactive oxygen species-sensitive biodegradable mesoporous Silica nanoparticles harboring TheraVac elicit tumor-specific immunity for Colon Tumor treatment, ACS Nano 17 (20) (2023) 19740–19752.
[67] Z. Pang, et al., MetaboAnalyst 5.0: narrowing the gap between raw spectra and functional insights, Nucleic Acids Res. 49 (W1) (2021) W388–w396.
[68] X. Zheng, et al., DNA nanotherapeutics facilitate efficient gynecological cancers treatment, J Control Release. 388 (2025) 114336.